nature communications

Article

https://doi.org/10.1038/s41467-025-60294-3

Cleavage of the Meckel-Gruber syndrome protein TMEM67 by ADAMTS9 uncouples Wnt signaling and ciliogenesis

Received: 16 September 2024

Accepted: 20 May 2025

Manu Ahmed[1], **Sydney Fischer**[1], **Karyn L. Robert**[1], **Karen I. Lange**[2], **Michael W. Stuck**[3], **Sunayna Best**[4,5], **Colin A. Johnson**[4], **Gregory J. Pazour**[3], **Oliver E. Blacque**[2] & **Sumeda Nandadasa**[1] ✉

TMEM67 mutations cause Meckel-Gruber syndrome and other related ciliopathies. TMEM67 is involved in both ciliary transition zone assembly, and non-canonical Wnt signaling mediated by its extracellular domain. How TMEM67 performs these two separate functions is not known. We identify a cleavage motif in the extracellular domain of TMEM67 cleaved by the extracellular matrix metalloproteinase ADAMTS9. This cleavage regulates the abundance of two functional forms: a C-terminal portion which localizes to the ciliary transition zone regulating ciliogenesis, and a non-cleaved form which regulates Wnt signaling. By characterizing three *TMEM67* ciliopathy patient variants within the cleavage motif utilizing mammalian cell culture and *C. elegans*, we show the cleavage motif is essential for cilia structure and function, highlighting its clinical significance. We generated a non-cleavable TMEM67 mouse model which develop severe ciliopathies phenocopying *Tmem67*$^{-/-}$ mice, but in contrast, transduces normal Wnt signaling, substantiating the existence of two functional forms of TMEM67.

Ciliopathies are a class of multi-organ developmental disorders caused by mutations affecting cilia formation or function. Frequently termed the 'antennae of the cell, primary cilia are immotile, singular (one per cell), microtubule-based signaling organelles that are present on almost all mammalian cell types[1–3]. The ciliary membrane is enriched with receptors that transduce signals in response to extracellular cues. These pattern the events of cellular differentiation, proliferation, and polarity, which together control tissue morphogenesis and organ formation during embryonic and postnatal development[4,5]. Motile cilia, on the other hand, can be both singular (node cilia) or formed in multiciliated epithelia, which regulate fluid flow dynamics in a variety of embryonic and postnatal tissue[6,7]. All cilia possess a specialized diffusion barrier, termed the transition zone (TZ), found at the base of the cilium. The TZ acts as a "gatekeeper" to regulate molecular traffic between the cilium and the cytoplasm[8,9]. The TZ is comprised of functional modules linked to ciliopathies, which are categorized based on genetic interactions and biochemical characterization. This includes the Meckel-Gruber syndrome (MKS) and nephronophthisis (NPHP) modules. Despite genetic and phenotypic overlap, these complexes have distinct spatial locations and interaction networks within the TZ[10–12].

MKS, first described by Johann Friedrich Meckel in 1822, is a relatively rare autosomal recessive disorder, with a 100% mortality rate[13]. MKS is characterized by large polycystic kidneys, polydactyly, and occipital encephalocele and represents the most severe end of the ciliopathy disease spectrum in humans[13–15]. Pathogenic variants in the transmembrane protein TMEM67 are the most frequent cause of MKS, linked to 16–20% of all clinically diagnosed MKS cases. *TMEM67* mutations also result in the medullary cystic kidney disease NPHP and

---

[1]Department of Pediatrics, University of Massachusetts Chan Medical School, Worcester, MA, USA. [2]School of Biomolecular & Biomedical Science, University College Dublin, Belfield, Ireland. [3]Program in Molecular Medicine, University of Massachusetts Chan Medical School, Worcester, MA, USA. [4]Division of Molecular Medicine, Leeds Institute of Medical Research, The University of Leeds, Leeds, UK. [5]Department of Clinical Genetics, Leeds Teaching Hospitals NHS Trust, Leeds, UK. ✉e-mail: Sumeda.Nandadasa@Umassmed.edu

Joubert syndrome (JBTS), a severe neurodevelopmental disorder characterized by a pathognomonic cerebellar and brain stem malformation known as the molar tooth sign[16–20].

TMEM67 variants also result in RHYNS syndrome, associated with retinitis pigmentosa, hypopituitarism, nephronophthisis, and skeletal dysplasia[21], as well as COACH syndrome, which is characterized by cerebellar vermis hypoplasia, oligophrenia, ataxia, coloboma, and hepatic defects[22–24]. The large number and the severity of these genetic disorders caused by *TMEM67* mutations underscore the central biological role played by TMEM67 in human development and health. TMEM67 is a component of the MKS module of the ciliary TZ, which forms part of the transition zone "necklace", composed of transmembrane and extracellular components of the TZ. These anchor the ciliary membrane to the Y-linkers and the microtubule core, and form a functional diffusion barrier[8]. However, TMEM67 is also comprised of an extracellular cysteine-rich domain (CRD) at its very N-terminus, which is homologous to the CRDs found in the Frizzled family receptors and the ROR family of receptor tyrosine kinases, which bind the Wnt ligands, modulating both canonical and non-canonical Wnt signaling pathways[25]. Previous work has shown that TMEM67 CRD binds to Wnt5a and forms a complex with ROR2, a co-receptor for non-canonical Wnt signaling, resulting in ROR2 phosphorylation and the transmission of non-canonical Wnt signaling[26–29]. In the absence of TMEM67/ROR2-mediated non-canonical Wnt signaling, mouse brains and kidneys show highly elevated canonical Wnt signaling, and therefore, TMEM67 function is crucial for regulating balanced canonical and non-canonical Wnt signaling during mouse development[26,29]. How TMEM67 controls both TZ assembly and Wnt signaling and what factors govern each function are unknown, and there is a corresponding lack in the understanding of the molecular mechanism(s) underlying the ciliopathies caused by *TMEM67* loss-of-function in humans.

We previously identified the extracellular matrix metalloprotease ADAMTS9 (A Disintegrin and Metalloproteinase with Thrombospondin motifs, family member 9) as a ciliopathy locus, resulting in NPHP and JBTS[30]. ADAMTS9 is necessary for normal ciliogenesis and TZ assembly in humans and mice[31]. Catalytically active ADAMTS9 is highly concentrated at the base of the cilium in Rab11+ endocytic recycling vesicles, carrying cilia-bound cargo. This localization requires the cell surface receptors LRP-1/2, clathrin-mediated endocytosis, and the recycling endosome to traffic ADAMTS9 into periciliary vesicles. ADAMTS9's catalytic function is also crucial for ciliogenesis, as catalytically inactive ADAMTS9 does not rescue the loss of ciliogenesis of *ADAMTS9*-null retinal pigment epithelial cells (RPE-1)[31]. However, the ADAMTS9 targets involved in ciliogenesis were unknown.

To answer this question, we undertook an advanced proteomics screen utilizing the iTRAQ TAILS N-Terminomics technique[32], and identified ADAMTS9 substrates[33]. Here, we unveil two ADAMTS9 cleavage sites present in the N-terminal extracellular domain of TMEM67. We show that TMEM67 has two functional forms governed by this proteolytic cleavage, one regulating Wnt signaling and a second regulating ciliary TZ assembly. We present a non-cleavable *Tmem67* mouse model, which is defective for ciliogenesis but in stark contrast to *Tmem67*-null, undergoes normal non-canonical and canonical Wnt signaling. Our work identifies a cellular mechanism in which the extracellular matrix-degrading metalloproteinase ADAMTS9 modifies the function of TMEM67, from a non-canonical Wnt signaling co-receptor at the cell surface, to a TZ scaffold protein, thereby uncoupling the dual functionality of TMEM67 in Wnt signaling and cilia formation.

Results

TMEM67 cleavage by the extracellular matrix metalloprotease ADAMTS9

To identify proteolytic substrates of ADMTS9 involved in ciliogenesis, we carried out an N-terminomics proteomics study utilizing the Terminal Amine Isotopic Labeling of Substrates (TAILS) technique[32], comparing *wild-type* (*Wt*) and *ADAMTS9*-null RPE-1 cells[33]. This highly specialized advanced proteomics approach, allowed us to label the neo N-termini generated by proteolytic cleavage of a protein utilizing isobaric tags and quantify N-terminal labeled peptide abundance by LC–MS/MS after their specific enrichment using a hyperbranched polyglycerol-aldehyde polymer (HPG-ALD) (Supplementary Fig. 1). Amongst a handful of known extracellular matrix substrates of ADAMTS9, the study revealed only one additional substrate known to be a structural component of the cilium, TMEM67. Mapping of the TMEM67 neo-peptide identified two highly conserved cleavage sites in the extracellular domain of TMEM67 occurring at K^{331}-F^{332} and N^{342}-F^{343}, which we named cleavage site 1 and 2 respectively (Fig. 1a). The F^{332} -labeled, non-tryptic 11 amino acid peptide released by the two cleavage events was either completely lost or present at significantly low abundance in *ADAMTS9* KO medium (Fig. 1b). Mapping the identified peptide in AlphaFold revealed the cleavage to occur at the end of a long linker region predicted to be in between the cysteine-rich domain (CRD) and the β-sheet-rich domain (BRD) (Fig. 1a). The two cleavage sites and the 11 amino acid sequence in between were also highly conserved across mammals (Fig. 1c). During the course of this study, the cryo-electron structure for TMEM67 was resolved at 3.3 Å resolution[34]. This revealed a homodimeric structure with 4 dimerization interfaces, in which the N-terminal extracellular domain of one protomer interacted with the BRD and the CRD of the second protomer, forming an extracellular arch[34]. Modeling the N-terminomics-identified cleavage sites in this cryo-EM structure revealed the cleavage to occur at the very N-terminus of the first homodimer interface, releasing a CRD-CRD dimer when cleaved (Supplementary Fig. 2a, b). The cryo-EM structure also revealed that the cleavage sites were in two previously uncharacterized, highly accessible, long linker regions located between the CRD and BRD of the TMEM67 extracellular domain, which we have named linker-1 (L_1) and linker-2 (L_2) respectively (Supplementary Fig. 2c, d, Fig. 1d). These unique characteristics gave us high confidence in further characterizing and validating the N-terminomics identified cleavage sites of TMEM67 utilizing N- and C-terminal-specific antibodies (Fig. 1d). Proteomics data predicted that a 34 kDa N-terminal fragment would be shed by TMEM67 extracellular domain cleavage. Western blotting of serum-free conditioned medium (incubated for 72 h) and the cell layers of *Wt* and *ADAMTS9*-null RPE-1 cells[31] utilizing the TMEM67 commercial antibody, validated this predication and revealed two closely migrating bands present only in the *Wt* medium and absent in the *ADAMTS9*-null medium, while the respective cell lysates showed the full-length TMEM67 (~120 kDa) to be more abundant in the *ADAMTS9*-null cells (Fig. 1e). Immunostaining with N- or C-terminal-specific TMEM67 antibodies[27], in *Wt* and *ADAMTS9*-null RPE-1 cells showed that only the TMEM67 C-terminus co-localized with the mature basal body marker CEP170, which marks the sub-distal appendages, in serum-starved *Wt* RPE-1 cells. Neither the TMEM67 N-terminus nor the C-terminus co-localized with the mature basal body in *ADAMTS9*-deficient cells (Fig. 1f–h). Co-staining with the Golgi marker GM130 showed TMEM67 N and -C-terminal staining in the secretory pathway in both cell lines and increased staining throughout *ADAMTS9* KO cells (Supplementary Fig. 3a, b). To investigate if the increased TMEM67 is at the cell surface, we performed immunostaining utilizing the TMEM67 N antibody and the cell surface marker wheat germ agglutinin (WGA) under non-permeable cell surface labeling which showed significantly higher levels of TMEM67 N labeling in *ADAMTS9* KO RPE-1 cells (Fig. 1i). Combined, these data suggest that only the TMEM67 C-terminal half, generated by cleavage, may be present at the ciliary TZ and increased TMEM67 present at the cell surface of *ADAMTS9* KO cells.

Removal of the TMEM67 N-terminus is required for ciliogenesis

To investigate the requirement for TMEM67 cleavage on ciliogenesis, we generated mammalian expression constructs for full-length

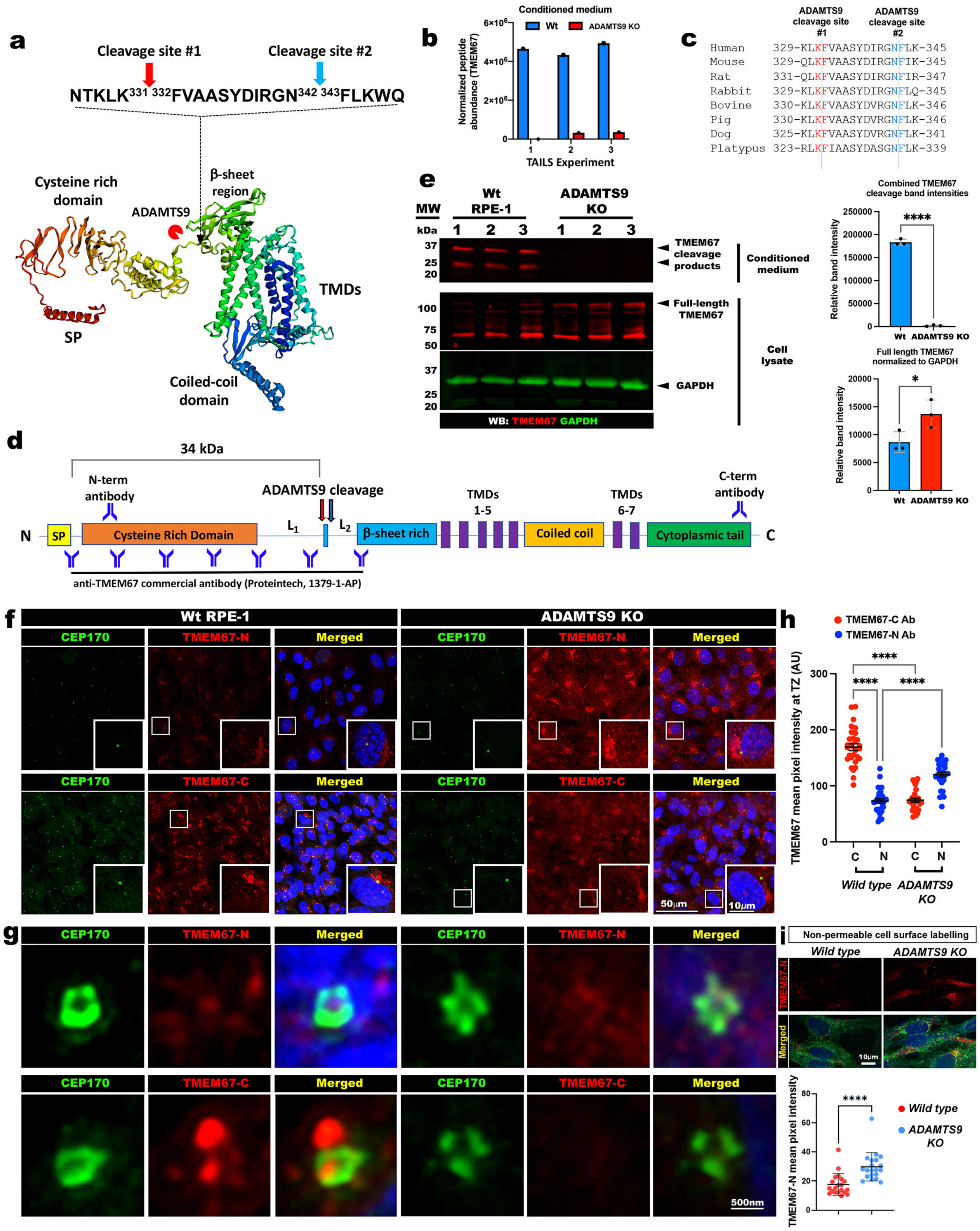

(TMEM67-FL), the C-terminal half resulting from ADAMTS9 cleavage (TMEM67 Δ342), the N-terminal CRD fragment shed by ADAMTS9 cleavage (TMEM67 N-331), and non-cleavable TMEM67, in which both (S1 + S2) or individual cleavage sites were mutated into alanine residues (Fig. 2a). Importantly, TMEM67 Δ342 was cloned into pSecTag2c, adding a signal peptide N-terminal to F^{343} to retain the correct topology of the cleaved TMEM67 C-terminal fragment. Loss of ciliogenesis in *TMEM67* KO RPE-1 cells was rescued by the transfection of full-length TMEM67 or TMEM67 Δ342 but not by TMEM67 N-331 or by the cleavage site mutants (S1, S2, S1 + S2) (Fig. 2b, c). Loss of ciliogenesis in *ADAMTS9*-null RPE-1 cells could also be partially restored by introducing TMEM67 Δ342 (Fig. 2d, e). These data together indicate that TMEM67 cleavage is required for ciliogenesis and that the TMEM67 C-terminal half (TMEM67 Δ342) generated by ADAMTS9-mediated

Fig. 1 | Identification and validation of TMEM67 as a substrate of ADAMTS9. **a** AlphaFold model of TMEM67 indicating the two ADAMTS9 cleavage sites identified utilizing N-terminomics in a linker region in between the cysteine-rich domain (CRD) and the β-sheet-rich domain (BRD) of TMEM67. **b** TMEM67 ^{332}FVAASYDRGN^{342} peptide abundance from three TAILS experiments, *Wt* (blue) and *ADAMTS9* KO (red). **c** TMEM67 sequence alignment showing conservation of the identified cleavage residues throughout mammalians. **d** TMEM67 domain structure, indicating the two ADAMTS9 cleavage sites, the newly identified linkers-1 and -2, the binding sites of N- and C-terminal TMEM67 antibodies, and the TMEM67 commercial antibody. **e** Western blot utilizing the TMEM67 commercial antibody (red) and GAPDH (green) from serum-free conditioned medium and cell layers. **** indicates a p-value < 0.0001, *<0.05 ($p = 0.0494$) in unpaired two-tailed Student's t-test. Samples collected from 3 independent biological replicates are shown. Error bars indicate Mean ± S.D. **f**–**h** High resolution (**f**), or super-resolution confocal microscopy (**g**), showing co-immunostaining of TMEM67 N- or C-terminal specific antibodies (red) with the mature basal body marker CEP170 (green) in serum-starved RPE-1 cells (**h**). **** indicates a p-value < 0.0001 in Kruskal–Wallis test + Dunn's multiple comparison test for statistical significance. Error bars indicate Mean ± S.E.M. $n = 30$ cells. Data from a single representative experiment from 3 independent experiments are shown. **i** Non-permeable cell surface staining using the TMEM67 N antibody (red) and the cell surface marker wheat germ agglutin (WGA, green). $n = 20$ cells from each group. Data from a single representative experiment from 3 independent experiments are shown. **** indicates a p value < 0.0001 in a two-tailed Mann–Whitney test. Error bars indicate Mean ± S.D. Scale bars in (**f**) are 50 µm and 10 µm, 500 nm in (**g**), and 10 µm in (**i**).

cleavage is sufficient and necessary to restore ciliogenesis. We next asked whether TMEM67 cleavage is required for its TZ localization. Full-length TMEM67 and TMEM67 Δ342 exhibited TZ localization comparable to that of *Wt* cells, while TMEM67 N-331, or the cleavage site mutants (S1, S2, and S1 + S2), showed very little TZ localization (Fig. 2f, g). These data show that TMEM67 cleavage regulates its C-terminal localization to the TZ and ciliogenesis.

TMEM67 cleavage is required for the assembly of the MKS/B9 module

To gain insight into the molecular mechanism of how loss of TMEM67 cleavage affects ciliogenesis, we investigated how TMEM67 and ADAMTS9 loss affected TZ assembly. We performed a comprehensive immunostaining analysis of 14 TZ proteins in *Wt*, *TMEM67* KO, and *ADAMTS9* KO RPE-1 cells, utilizing high-resolution and super-resolution confocal microscopy to investigate their localization to the mature basal body upon ciliogenesis induction. Of the 14 TZ proteins examined, we found that 6 (TCTN1, TCTN2, TCTN3, TMEM237, CC2D2A, and B9D2) were significantly reduced in both *TMEM67* and *ADAMTS9* KO cells (Fig. 3a, b, Supplementary Fig. 4a–f and Supplementary Fig. 5a–h). In addition to these core changes, loss-of *ADMTS9* but not *TMEM67* significantly reduced B9D1, NPHP1, and NPHP5 and significantly increased CEP290 staining, while loss-of *TMEM67* but not *ADAMTS9* significantly increased RPGRIP1L and decreased INPP5E localization (Fig. 3b). Intensity of CEP170 was measured as a control and showed no significant change between the cell lines (Fig. 3b). We carried out western blotting and qRT-PCR analysis of the 6 MKS/B9 module proteins that were reduced in both cell lines, which showed total protein level for TCTN1 was also reduced in both *TMEM67* KO and *ADAMTS9* KO cells while B9D2 was reduced only in *TMEM67* KO cells (Fig. 3c, d). Their gene expression was not significantly decreased in *TMEM67* and *ADAMTS9 KO* cells compared to *Wt* cells, except *TCTN3* and *CC2D2A*, which showed reduced transcription in both cell lines (Fig. 3d). These results, summarized in the known TMEM67 interactome (Fig. 3e), shows loss-of *TMEM67* and ADAMTS9-proteolytic activity significantly affects the MKS/B9 module during TZ assembly.

TMEM67 Δ342 is sufficient for restoring transition zone assembly

Since loss of ciliogenesis in *TMEM67* KO and *ADAMTS9* KO cells can be rescued by TMEM67 Δ342, we tested whether it was sufficient to rescue the TZ MKS/B9 module. *TMEM67* KO cells transfected with TMEM67 Δ342 showed significantly increased levels of the 6 MKS/B9 proteins reduced from the TZs lacking TMEM67 (Fig. 4a, b). Analysis of TCTN1 and B9D2 protein levels by western blotting also showed these MKS module proteins which were significantly decreased in *TMEM67* KO cells can also be restored by TMEM67 Δ342 (Supplementary Fig. 6b). *ADAMTS9* KO cells transfected with TMEM67 Δ342 showed a similar result with significantly increased TZ pixel intensity for TCTN1, TCTN2, TCTN3, TMEM237, and CC2D2A with the exception of B9D2 (Fig. 4c, Supplementary Fig 6a). These results show that TMEM67 Δ342 is sufficient to rescue TZ assembly defects caused by loss of TMEM67 and, in part, in *ADAMTS9*-deficient cells. This suggests that release of the TMEM67 Δ342 fragment following ADAMTS9-mediated cleavage is an important regulatory mechanism governing the recruitment or stabilization of membrane-associated MKS/B9 components to the TZ.

TMEM67 variants surrounding the cleavage sites result in ciliopathies

Three *TMEM67* variants within or adjacent to the TMEM67 cleavage motif have been identified in ciliopathy patients (Fig. 4d). The c.1027T>G mutation corresponding to p.F343V, occurs at the second cleavage site and resulted in bilateral enlarged cystic kidneys, ductal plate malformation (DPM) of the liver and abnormal lung lobulation[35]. A c.986A>C mutation leading to p.K329T, two residues upstream of the first cleavage site, causes nephronophthisis (NPHP), ataxia, cerebellar vermis hypoplasia, mental retardation, and hepatic fibrosis[19]. The c.1046T>C mutation, corresponding to p.L349S, was identified in individuals across two families with biallelic *TMEM67* mutations, resulting in MKS, COACH syndrome, cleft palate, and intra-uterine growth retardation[17]. We tested whether these patient variants affect ciliogenesis by conducting rescue experiments in *TMEM67* KO RPE-1 cells. RPE-1 cells transfected with TMEM67 F343V, K329T, and L349S variants showed reduced ciliogenesis compared to *TMEM67* KO cells transfected with full-length TMEM67 (Fig. 4e–g). Western blot analysis for TMEM67 cleavage utilizing the TMEM67 commercial antibody showed all three variants were also defective for cleavage (Fig. 4h). We did not detect the less abundant lower molecular weight cleavage product during these transient transfection experiments, which utilized a 24 h incubation period post-transfection. All three patient variants also showed reduced TZ localization compared to cells transfected with the full-length TMEM67 construct (Fig. 4i, j). To investigate the MKS/B9 module formation by the patient variants we investigated the TZ localization of TCTN1-3, TMEM237, CC2DA and B9D2 immunostaining (Fig. 4k, Supplementary Fig. 6c). Compared to *TMEM67* KO cells transfected with full-length TMEM67 which restored MKS/B9 module formation, the patient variants showed significantly decreased staining of MKS/B9 module proteins. Since all three variants are in the two linker regions identified here, these results show that the cleavage residues and the correct formation of the two linker regions are critical to TMEM67 functionality during human development.

TMEM67 cleavage site is essential for *C. elegans* MKS-3 function

Using ConVarT sequence alignment tool[36], we found that the predicted cleavage sites occur within a highly conserved region of TMEM67 orthologs across diverse animals, including the small roundworm, *Caenorhabditis elegans* (Fig. 5a). AlphaFold[37] revealed that this region of the *C. elegans* ortholog (MKS-3) is on an outer face of the protein, consistent with its accessibility for extracellular protease cleavage (Fig. 5b). To determine if the predicted cleavage site is essential for MKS-3 function, CRISPR-Cas9 was used to engineer two variants: F249V that corresponds to the F343V patient variant of the second

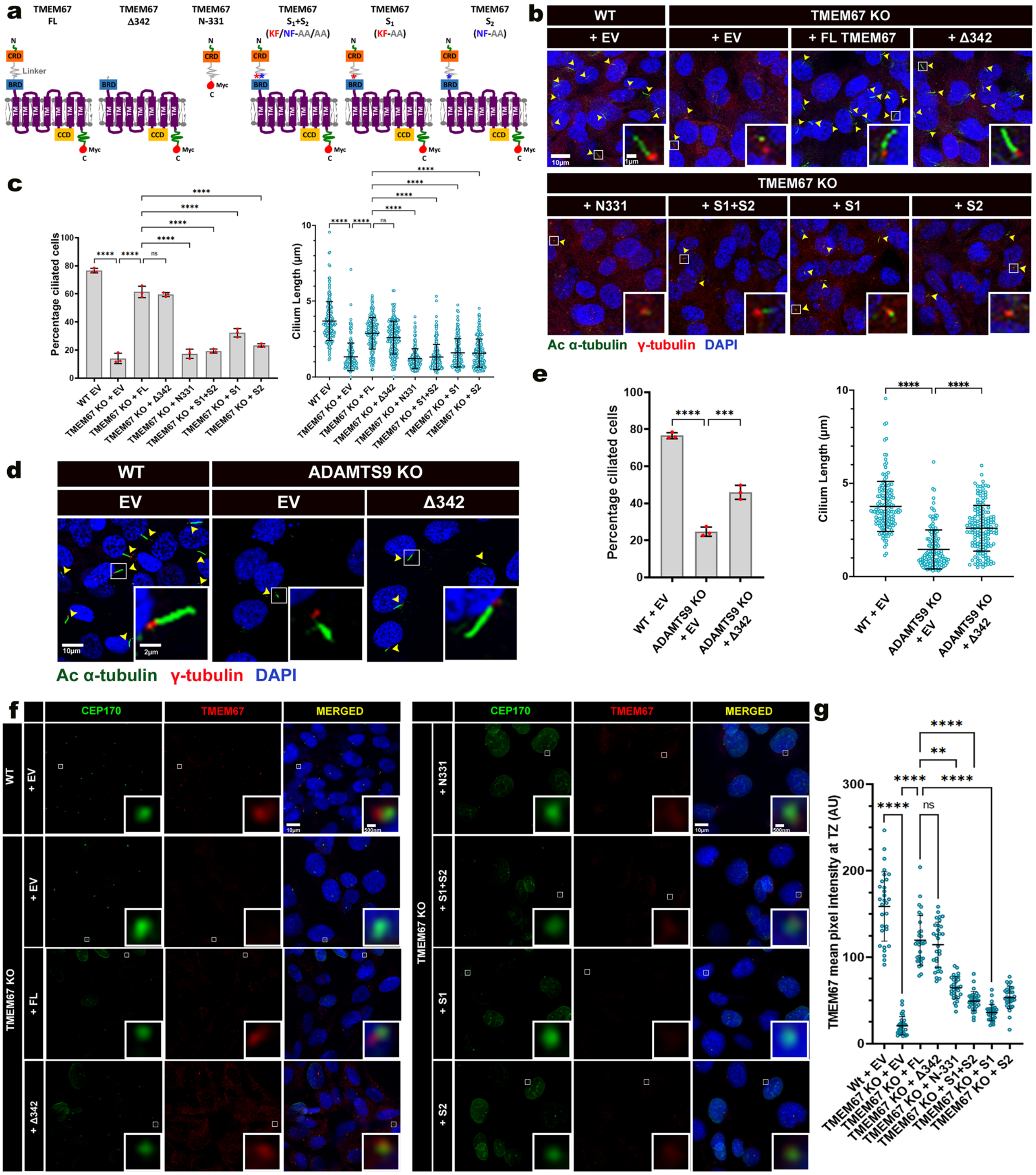

cleavage site, and *mks-3*(ΔCLE), which possesses four amino acid substitutions (L238A, F239A, T248A, F249A) predicted to abolish both cleavage sites and is similar to the human TMEM67 S1 + S2 construct. As the *mks-3* null mutant lacks severe phenotypic defects on account of functional redundancy between MKS and NPHP module genes[38,39], we conducted most of our *mks-3* variant assessments in worms harboring a background mutation in *nphp-4*. Using quantitative assays of cilia integrity (dye filling) and sensory behavior (roaming and chemotaxis)[28], we found that the F249V and ΔCLE mutations significantly disrupt cilia structure and function (Fig. 5c–e). Further analysis of cilium structure using a ciliary transmembrane protein reporter (TSP-6::mScarlet) expressed in phasmid (tail) neurons confirmed that the ΔCLE mutation causes a higher incidence of short cilia in worms harboring the *nphp-4* background mutation (Fig. 5f, g). To determine if the *mks-3* mutations affect the composition of the TZ, we quantified levels of the *C. elegans* ortholog of B9D2, MKSR-2, in single *mks-3* mutants and in the *mks-3; nphp-4* double mutants. Using an endogenously expressed reporter (mNG::MKSR-2), we found that although MKSR-2 was still recruited to the TZ of the *mks-3* mutants, its levels were significantly decreased in the null and ΔCLE alleles (Fig. 5h). In the *nphp-4* sensitized background the F249V mutation also significantly reduces mNG::MKSR-2 levels at the TZ (Fig. 5h). Interestingly, this data contradicts previous reports that observed *mks-3* loss does not affect the TZ localization of MKS module proteins[38,39]; however, those

Fig. 2 | ADAMTS9-mediated TMEM67 cleavage is required for ciliogenesis and TMEM67 TZ localization. a TMEM67 constructs generated encoding full-length TMEM67 (FL), the C-terminal cleavage product (Δ342), N-terminal cleavage product (N-331), dual cleavage mutant (S1 + S2), individual mutation of cleavage site-1 (S1) and cleavage site-2 (S2) alone. A signal peptide sequence was added at the N-terminus of the TMEM67 Δ342 construct, not indicated in the illustration. **b**, **c** *Wt* or TMEM67 KO RPE-1 cells transfected with the indicated TMEM67 constructs showing primary cilia (yellow arrowheads) by acetylated α-tubulin (green) and γ-tubulin (red) staining (EV empty vector). Percentage of ciliated cells ($n = 100$) and cilium length ($n = 150$) quantification from 3 independent experiments are shown in (**c**). One-way ANOVA + Sidak's multiple comparison test was used for the percentage of ciliated cells. **** indicates a p-value <0.0001; Kruskal–Wallis test + Dunn's multiple comparison test used for cilium length. **** indicates a p-value <0.0001. Error bars indicate Mean ± S.D. **d**, **e** TMEM67 Δ342 transfection partially rescues ciliogenesis and cilium length of *ADAMTS9* KO RPE-1 cells. Yellow arrowheads indicate primary cilia, acetylated α-tubulin (green), and γ-tubulin (red). Percentage of ciliated cells ($n = 100$) and cilium length quantification ($n = 150$) from 3 independent experiments are shown in (**e**). **** indicates a p-value <0.0001, ***<0.001 ($p = 0.0002$) in one-way ANOVA + Tukey's multiple comparison test in percentage ciliated cell quantification, and **** indicates a p-value <0.0001 in Kruskal–Wallis test + Sidak's multiple comparison test for cilium length. Error bars indicate Mean ± S.D. **f**, **g** TMEM67 commercial antibody (red) and CEP170 (green) immunostaining in *Wt* and *TMEM67* KO cells transfected with indicated TMEM67 constructs (**g**). $n = 30$ cells for each group. Data from a single representative experiment from 3 independent experiments are shown. **** indicates a p-value <0.0001, **<0.01 ($p = 0.0016$) in two-sided Kruskal–Wallis test + Dunn's multiple comparison test for statistical significance. Error bars indicate Mean ± S.D. Scale bars in (**b**, **d**, and **f**) are 10 µm and 1 µm in (**b**) insert, 2 µm in (**d**) insert, and 500 nm in (**f**) insert.

experiments were conducted with overexpressed reporters and not a knock-in endogenous reporter as used here. Taken together, these data show that human TMEM67 cleavage sites are essential for *C. elegans* MKS-3 ciliary functions. Whether the ancestral nematode ortholog of the mammalian ADAMTS9, GON-1[40], is also involved in MKS-3 cleavage remains to be determined.

Tmem67$^{\Delta CLE/\Delta CLE}$ mice phenocopy *Tmem67*-null mice

To investigate the role of TMEM67 cleavage in vivo, we developed a mouse model in which both the TMEM67 cleavage sites K^{331}/F^{332} (cleavage site-1) and N^{342}/F^{343} (cleavage site-2) were mutated to alanine residues (*Tmem67*$^{\Delta CLE/\Delta CLE}$, Supplementary Fig. 7a). Two independent founder lines, *Tmem67*$^{\Delta CLE1}$ and *Tmem67*$^{\Delta CLE2}$, were generated from two independent mouse ES cell clones in the C57BL6/j background (Supplementary Fig. 7a). Homozygous mice from both lines were phenotypically identical and here forth will be commonly referred to as *Tmem67*$^{\Delta CLE/\Delta CLE}$ mice. *Tmem67*$^{\Delta CLE/\Delta CLE}$ mice only survived till postnatal day 14 (p14) and phenocopied *Tmem67-null* mice, developing large polycystic kidneys (10/10 mice) and hydrocephaly (10/10 mice) with significantly impaired postnatal growth (Fig. 6a–c, Supplementary Fig. 8a and Supplementary Fig. 9a–c). The *Tmem67*$^{\Delta CLE/+}$ (heterozygous) mice were phenotypically normal and showed normal kidney histology at 10 weeks of age (p70, Supplementary Fig. 8b). The vast majority of *Tmem67*$^{\Delta CLE/\Delta CLE}$ mice exhibited embryonic lethality similar to *Tmem67* KO mice[27], and showed defective cardiac, hepatic and vascular phenotypes (Supplementary Fig. 8a, c, d). *Tmem67*$^{\Delta CLE/\Delta CLE}$ hearts from E15.5 and E18.5 embryos revealed severely impaired cardiac development, resulting in an overriding aorta, ventricular septal defect (VSD), and a loss of myocardial compaction (Supplementary Fig. 8d). Livers from postnatal *Tmem67*$^{\Delta CLE/\Delta CLE}$ mice showed defective hepatic portal vein (HPV) branching morphogenesis, loss of hepatocyte differentiation, and increased fibrosis (Supplementary Fig. 9e–g). Freeze-fracture scanning electron microscopy (SEM) revealed *Tmem67*$^{\Delta CLE/\Delta CLE}$ cystic renal tubular epithelium had severely shortened, malformed primary cilia (turquoise arrows), as well as extended primary cilia which were morphologically abnormal (orange arrows), similar to that seen in *Tmem67*-null kidneys (Fig. 6d). The cystic kidney samples show large, open "pit-like" surfaces facilitating *en face* imaging. However, in the healthy *Wt* kidney, the renal cilia could only be visualized residing inside the narrow tubules with a limited imaging angle. Transmission electron microscopy (TEM) of both short and long cilia showed a complete loss-of the TZ necklace formation, seen in the *Wt* littermate kidney primary cilia (red arrowheads, Fig. 6e, Supplementary Fig. 10a). Quantification of renal cilia lengths from SEM images showed the presence of both severely short and long cilia in *Tmem67-null* and *Tmem67*$^{\Delta CLE/\Delta CLE}$ cystic renal tubular epithelium (Supplementary Fig. 10b). Loss-of TMEM67 results in hydrocephaly in humans, mice, rat, and zebrafish[26,41–43]. Analysis of the multiciliated ependymal epithelium lining the lateral brain ventricles showed an overall decrease in ciliogenesis (Supplementary Fig. 10c) and highly abnormal motile cilia in the *Tmem67*$^{\Delta CLE/\Delta CLE}$ mice (Fig. 6f). Nearly all the motile cilia observed contained bulbous tips and large membrane-bulges either at the distal ends or on their sides (yellow arrowheads, Fig. 6f). Compared to the well-organized motile cilia observed in *Wt* brains, the ependymal cilia of the *Tmem67*$^{\Delta CLE/\Delta CLE}$ were tangled and laid flat on the surface (Fig. 6f). Low magnification SEM images also revealed the presence of large white blood cells in the ependymal layer, indicative of high immune activity in the mutant brain ventricles (Supplementary Fig. 10c). TEM images of the mutant motile cilia phenocopied the renal primary cilia and showed a complete loss-of the TZ necklace (red arrowheads, Fig. 6g). These results validated our in vitro findings, analyzing *TMEM67* and *ADAMTS9*-null RPE-1 cells. These data also show that TMEM67 cleavage is essential for normal mammalian development and the normal morphogenesis of the TZ in primary and motile cilia, and its loss leads to multi-organ failure in mice. Crucially, since *Tmem67*$^{\Delta CLE/\Delta CLE}$ mice are phenotypically identical to *Tmem67*-null, it also suggests that TMEM67 loss-of-cleavage results in a nonfunctional TMEM67.

Non-cleavable TMEM67 maintains Wnt signaling but does not localize to the TZ

To investigate the functionality of the TMEM67-ΔCLE protein, we harvested and immortalized mouse embryonic fibroblasts (MEFs) from E13.5 *Tmem67*$^{\Delta CLE/\Delta CLE}$ embryos. Following serum starvation, *Tmem67*$^{\Delta CLE/\Delta CLE}$ MEFs had significantly reduced ciliogenesis and cilia lengths compared to littermate *Tmem67*$^{\Delta CLE/+}$ MEFs (Fig. 7a, b, Supplementary Fig. 10d, e). TZ localization of TMEM67 was also lost in *Tmem67*$^{\Delta CLE/\Delta CLE}$ MEFs (Fig. 7c), supporting the observation that human TMEM67-S1+ S2 did not rescue ciliogenesis and lacked TZ localization (Fig. 2f). Transfection of the TMEM67 C-terminal half (TMEM67 Δ342) significantly improved the loss of ciliogenesis and cilia lengths of *Tmem67*$^{\Delta CLE/\Delta CLE}$ MEFs (Fig. 7d, e). Western blot analysis of the serum-free conditioned medium revealed a ~34 kDa TMEM67 cleavage product produced by *Wt* but not by *Tmem67*$^{\Delta CLE/\Delta CLE}$ MEFs, with more full-length TMEM67 in the *Tmem67*$^{\Delta CLE/\Delta CLE}$ cell lysates (Fig. 7f). To visualize TMEM67-ΔCLE protein expression on the cell surface, we immunostained *Wt* and *Tmem67*$^{\Delta CLE/\Delta CLE}$ MEFs under non-permeable cell surface labeling conditions utilizing the TMEM67 N antibody together with the cell surface marker WGA (Supplementary Fig. 11a), which revealed significantly more TMEM67 present on the surface of *Tmem67*$^{\Delta CLE/\Delta CLE}$ MEFs (Supplementary Fig. 11b). qRT-PCR analysis for *Tmem67* transcript levels showed similar abundance in MEFs (Fig. 7g) and whole kidneys (Supplementary Fig. 7c), which showed *Tmem67* transcription is unaffected in *Tmem67*$^{\Delta CLE/\Delta CLE}$ mice. Combined, these data validated the *Tmem67*$^{\Delta CLE/\Delta CLE}$ mouse model's ability to produce a non-cleavable form of TMEM67 that lacks ciliary TZ localization and TZ assembly.

Since the *Tmem67*$^{\Delta CLE/\Delta CLE}$ mice phenocopied *Tmem67*-null mice, we reasoned that further investigation of this model would yield new

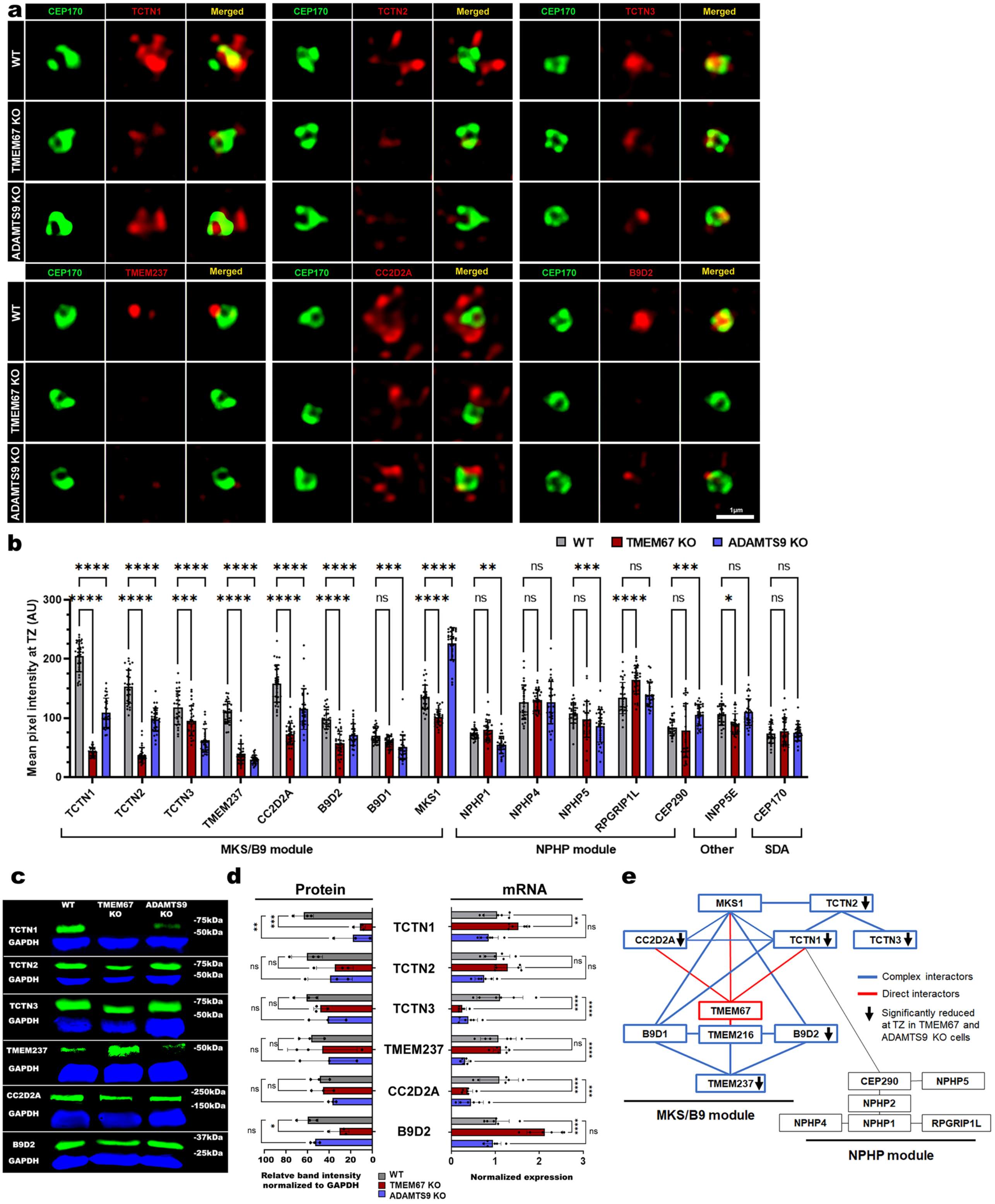

insights into the mechanism by which *TMEM67* mutations cause ciliopathies. The cysteine-rich domain (CRD), present in the TMEM67 extracellular domain shed by ADAMTS9, is highly homologous to the CRDs of the Wnt ligand binding Frizzled receptors[26], and TMEM67 has been implicated in the modulation of both canonical and non-canonical Wnt signaling pathways[24,26–29,44]. In particular, the TMEM67 extracellular domain is required for the activation of the non-canonical Wnt signaling pathway, forming a direct complex with Wnt5a and the non-canonical Wnt signaling receptor ROR2, and is required for phosphorylating ROR2 upon Wnt5a treatment[27,28]. First, we tested whether the non-cleavable TMEM67-ΔCLE form could transduce non-canonical Wnt signaling by analyzing ROR2 phosphorylation in vitro (Fig. 7h). We found that, upon Wnt5a treatment, *Tmem67*$^{\Delta CLE/\Delta CLE}$ MEFs phosphorylated ROR2, similar to *Wt* but dissimilar to *Tmem67-null* MEFs, which failed to do so. Second, to investigate the Wnt signaling signature in vivo, we analyzed the ependymal cells lining the brain ventricles of postnatal day 14 *Wt*, *Tmem67*-null, and *Tmem67*$^{\Delta CLE/\Delta CLE}$ mice (Fig. 7i). Active β-catenin staining revealed elevated active

Fig. 3 | Loss of TMEM67 or ADAMTS9 severely impairs transition zone assembly in RPE-1 cells. **a** Super-resolution microscopy images of the transition zone MKS/B9 module proteins (red) and CEP170 (green) in *Wt*, *ADAMTS9* KO, and *TMEM67* KO RPE-1 cells. **b** Mean pixel intensity quantification of all 14 transition zone proteins analyzed in this study, comparing *Wt*, *TMEM67* KO, and *ADAMTS9* KO RPE-1 cells ($n = 30$, each group per experiment), data from a single representative experiment from 3 independent experiments are shown. **** indicates a *p*-value <0.0001, ***<0.001, **<0.01, *<0.05 in two-way ANOVA test + Dunnet's multiple comparison test. Error bars indicate Mean ± S.D. $p = 0.0009$(B9D1, *Wt* vs *ADAMTS9* KO); $p = 0.0023$(NPHP1, *Wt* vs *ADAMTS9 KO*); $p = 0.0003$(NPHP5, *Wt* vs *ADAMTS9* KO); $p = 0.512$(RPGRIP1L, *Wt* vs *ADAMTS9* KO); $p = 0.0007$(CEP290, *Wt* vs *ADAMTS9* KO); $p = 0.0106$(INPP5E, *Wt* vs *TMEM67* KO); $p = 0.0002$(TCTN3, *Wt* vs *TMEM67* KO). **c**, **d** Western blot and qRT-PCR analysis of TCTN1, TCTN2, TCTN3, TMEM237, CC2D2A and B9D2 (green) in *Wt*, *TMEM67* KO and *ADAMTS9* KO RPE-1 cells. Data from 3 independent experiments are shown. **** indicates a *p*-value <0.0001, ***<0.001, **<0.01, *<0.05 in two-way ANOVA + Dunnet's multiple comparison test for statistical significance (**d**). Error bars indicate Mean ± S.D. In protein analysis, $p = 0.0003$(TCTN1, *Wt* vs *TMEM67* KO), $p = 0.0013$(TCTN1, *Wt* vs *ADAMTS9* KO), $p = 0.04$(B9D2, *Wt* vs *TMEM67* KO), in mRNA analysis, $p = 0.0084$(*TCTN1*, *Wt* vs *TMEM67* KO), $p = 0.0004$(*CC2D2A*, *Wt* vs *ADAMTS9* KO), **e** Graphical representation of the TZ protein interaction network in relation to TMEM67 (red box). TMEM67 direct interactions are shown in red lines, while interactions amongst the four direct interactors are shown in blue lines. MKS/B9 module proteins are shown in blue boxes, while the NPHP module proteins are shown in black boxes. Black arrows indicate significantly reduced TZ proteins in both *TMEM67* KO and *ADAMTS9* KO cells. Scale bar in (**a**) is 1 μm.

β-catenin staining in *Tmem67*-null brains, presumably due to the loss-of the non-canonical Wnt signaling pathway, but in contrast, normal levels of active β-catenin staining were seen in *Tmem67*$^{\Delta CLE/\Delta CLE}$ brains (Fig. 7i). Immunostaining for the basal body marker FOP (fibroblast growth factor receptor-1 oncogene partner) revealed unaltered apical localization of the basal bodies in *Tmem67*$^{\Delta CLE/\Delta CLE}$ and *Tmem67-null* brain ventricles (Fig. 7i).

Immunostaining for active β-catenin and F-actin upon Wnt3a or Wnt5a treatment of MEFs revealed increased active β-catenin staining and its nuclear localization upon activation of the canonical Wnt signaling pathway, and increased F-actin staining upon activation of the non-canonical Wnt signaling pathway, in both *Tmem67*$^{\Delta CLE/+}$ and *Tmem67*$^{\Delta CLE/\Delta CLE}$ MEFs (Fig. 8a–d). qRT-PCR analysis of canonical and non-canonical Wnt signaling markers also revealed that *Tmem67*$^{\Delta CLE/\Delta CLE}$ MEFs transduced both signaling pathways as expected (Fig. 8e, f), while *Tmem67-null* MEFs failed to upregulate non-canonical Wnt target genes upon Wnt5a treatment but surprisingly upregulated canonical Wnt targets in response to Wnt5a (*Tcf7, Jun, Myc, and Ccnd1*). These results supported the observations of dysregulated Wnt signaling seen in *Tmem67-null* tissues by others and reported here (Fig. 7i). *Tmem67* transcription itself was also regulated by canonical and non-canonical Wnt signaling in *Wt* and *Tmem67*$^{\Delta CLE/\Delta CLE}$ MEFs (Fig. 8g).

Combined, these results show that TMEM67 is indeed involved in regulating both normal Wnt signaling and ciliogenesis, supporting the findings of previous studies. Our findings provide the molecular mechanism by which TMEM67 performs these two functions (Fig. 9a). Cleavage by an extracellular matrix metalloproteinase generates the N-terminally cleaved TMEM67 (TMEM67 Δ342 form), which functions at the TZ and is required for normal assembly of the TZ necklace, while the full-length or the non-cleavable form (TMEM67-ΔCLE) is required to regulate Wnt signaling. More importantly, these data also suggest that the molecular mechanisms of the ciliopathies caused by TMEM67 loss-of-function are due to loss-of its TZ activity and not by its Wnt signaling activity, which could only be elucidated by the generation of the *Tmem67*$^{\Delta CLE/\Delta CLE}$ mice, which show defective ciliogenesis but normal Wnt signaling, whereas *Tmem67*-null are defective in both (Fig. 9b).

Discussion

Here we have uncovered an evolutionarily conserved cleavage motif present in the extracellular domain of the Meckel-Gruber syndrome protein TMEM67, revealing the molecular mechanism regulating the formation of two functional isoforms by the extracellular metalloproteinase ADAMTS9. First, a C-terminal cleaved form, localized in the ciliary TZ, is involved in the formation of the TZ necklace and MKS/B9 module assembly. We suggest that loss of this cleaved TMEM67 C-terminal fragment from the TZ is the underlying disease-causing mechanism disrupted in ciliopathies, both in *Tmem67*$^{\Delta CLE/\Delta CLE}$ mice and, presumably, in humans with loss-of-function mutations. Second, the full-length non-cleaved form is essential for regulating Wnt signaling. ADAMTS9-mediated cleavage of TMEM67 regulates the abundance of each isoform and their respective functions and sub-cellular localizations (Fig. 9a). Whether the released N-terminal fragment containing the CRD can augment Wnt signaling acting long-range and non-cell autonomously, remains to be determined. Our work suggests that the TMEM67 N-terminus needs to be proteolytically removed as a prerequisite for TZ localization of the C-terminus and cilium assembly. This is equivalent to a “pro-domain” present in many secreted enzymes, which require proteolytic removal for their full functionality. Intracellular trafficking networks, signal peptides, and post-translational modifications (PTMs) are all known to facilitate the trafficking of molecules to the correct sub-cellular location. Our work shows that removal of the TMEM67 N-terminus by ADAMTS9 is critical for the correct ciliary targeting of TMEM67, whereas the full-length protein exhibits a distinct localization pattern on the cell membrane and Golgi. Whether ADAMTS9-mediated cleavage causes TMEM67 C-terminal endocytosis and TZ localization via endocytic recycling or causes lateral diffusion within the cell membrane during cilium assembly also remains unknown (Fig. 9a).

Previous studies from other groups have shown that proteolytic cleavage is a prerequisite for ciliary localization of the transmembrane protein Polycystin-1 (PC1), and mutations of the extracellular domain cleavage site can also cause autosomal dominant polycystic kidney disease[45–49]. For the PC1/PC2 complex to be effectively targeted to the cilium, PC1 is autoproteolytically cleaved at a G-protein coupled receptor cleavage site (GPS) during trafficking[50], but the exact molecules involved are unknown. Here we show that extracellular matrix metalloproteinases can facilitate transmembrane protein trafficking to the ciliary membrane. Since TMEM67 Δ342 only partially rescues ciliogenesis of *ADAMTS9*-null RPE-1 cells, most likely ADAMTS9 and its homologous sister protease, ADAMTS20, may be involved in proteolytically cleaving other extracellular proteins essential for ciliogenesis. Since *Adamts9* and *Adamts20* are not ubiquitously expressed[51], whether additional extracellular proteases can cleave the TMEM67 extracellular domain in different tissues in mammals is also unknown.

Our comprehensive immunostaining analysis of 14 bona fide TZ proteins revealed that 6 MKS/B9 proteins were reduced or lost at the TZ in both *TMEM67* and *ADAMTS9* KO cells, while components of the NPHP module were mostly unaffected. Analysis of *Tmem67*$^{\Delta CLE/\Delta CLE}$ primary cilia and motile cilia by TEM revealed that the TZ necklace is missing upon loss of TMEM67 cleavage. Loss of TCTN1 from photoreceptor cilia also prevents ciliary necklace formation and the TZ gatekeeping activity[52], highlighting the significant role played by the extracellular and transmembrane components of the TZ. Previous super-resolution microscopy studies revealed that NPHP proteins exhibit a narrower diameter located towards the microtubules, while the MKS complex proteins occupy a wider region towards the ciliary membrane[53,54]. Here we show that the wider MKS/B9 proteins are lost or reduced in *TMEM67* KO cells, while TZ proteins belonging to the NPHP module are unaffected. We therefore propose that TZ assembly may be initiated in an inside-out manner from the axonemal microtubules to the membrane, as proteins lost in *TMEM67* KO cells also

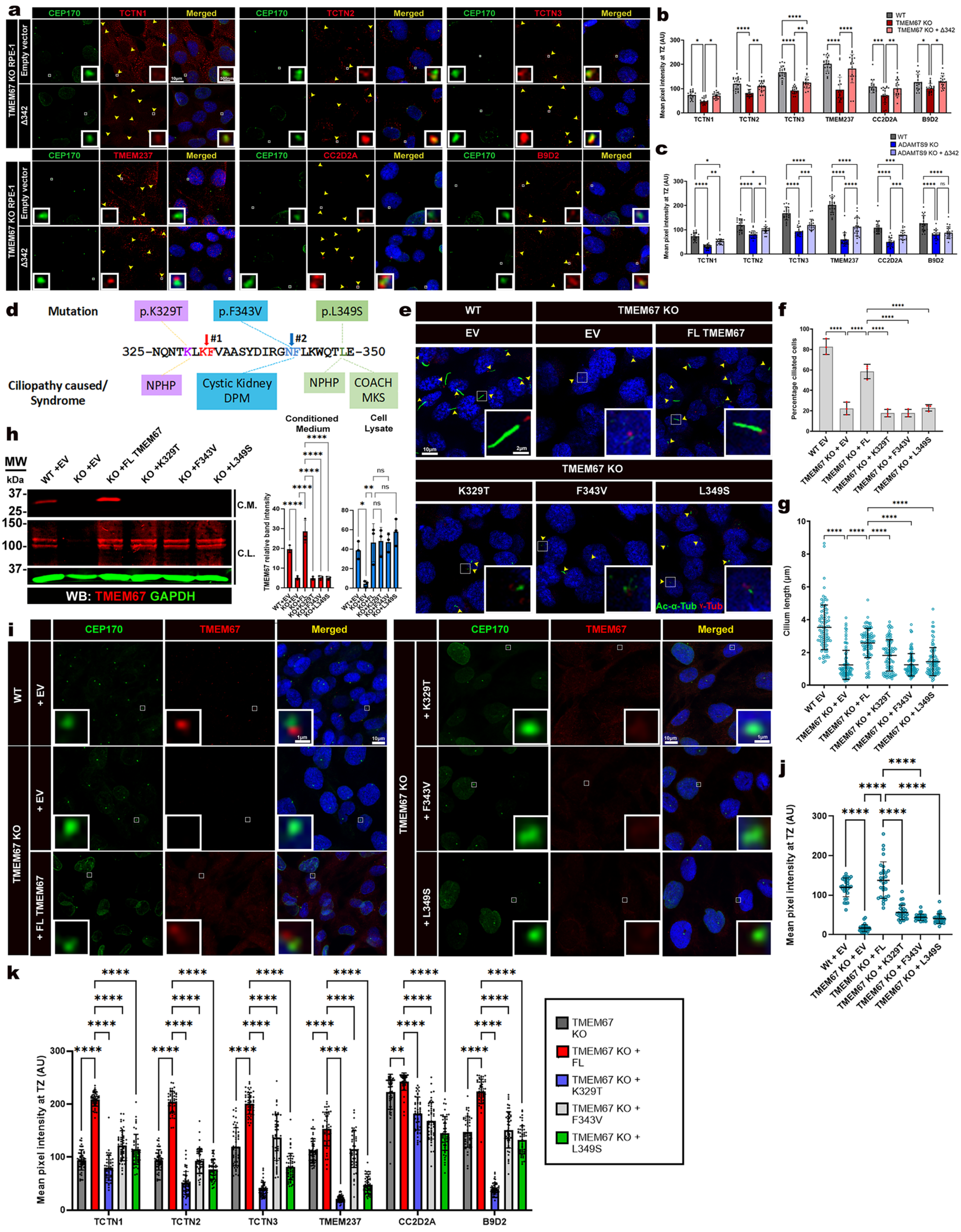

exhibit a wider axial diameter. Secondly, TZ assembly may also be occurring in a modular fashion, where NPHP and MKS modules are assembled independently. Future in-depth studies probing this specific question are required to confirm this, however, and this study provides a basis to better understand the molecular hierarchy of ciliary TZ proteins in relation to TMEM67. Furthermore, the functional domains and motifs also relate to their location within the TZ. NPHP proteins are enriched in microtubule-binding domains and coiled-coil motifs in comparison to MKS proteins, which comprise the cell membrane-binding (B9, C2), transmembrane, and extracellular domains. CEP290 and RPGRIP1L are enriched in coiled-coil motifs and are known to be coordinators of TZ assembly, with CEP290 interacting with proteins from both the NPHP and MKS modules[8,38,55,56]. Our findings support the notion that TMEM67 plays a central role in anchoring

Fig. 4 | TMEM67 Δ342 can restore TZ assembly and ciliopathy variants within the cleavage residues that affect cleavage. **a** TZ proteins (red) and CEP170 (green) in *TMEM67* KO cells transfected with empty vector (EV) or TMEM67 Δ342. TZ are indicated by yellow arrowheads, boxed areas are in inserts. **b**, **c** TZ mean pixel intensities ($n = 20$ cells per group). Data from a single representative experiment from 3 independent experiments are shown. **** indicates a p-value <0.0001, ***<0.001, **<0.01, *<0.05 in two-way ANOVA + Tukey's multiple comparison test for statistical significance. $p = 0.0166$(TCTN1, *Wt* vs *TMEM67* KO); $p = 0.0342$(TCTN1, *TMEM67* KO vs *TMEM67* KO + Δ342); $p = 0.0048$(TCTN2, *TMEM67* KO vs +Δ342); $p = 0.0016$(TCTN3, *TMEM67* KO vs *TMEM67* KO + Δ342); $p = 0.0002$(CC2D2A, *Wt* vs *TMEM67* KO), $p = 0.0039$(CC2D2A, *TMEM67* KO vs *TMEM67* KO + Δ342); $p = 0.0157$ (B9D2, *Wt* vs *TMEM67* KO), $p = 0.0100$(B9D2, *TMEM67* KO vs *TMEM67* KO + Δ342); $p = 0.0144$(TCTN1, *Wt* vs *ADAMTS9* KO + Δ342), $p = 0.0071$(TCTN1, *ADAMTS9* KO vs *ADAMTS9* KO + Δ342); $p = 0.0133$(TCTN2, *Wt* vs *ADAMTS9* KO + Δ342); $p = 0.0285$ (TCTN2, *ADAMTS9* KO vs *ADAMTS9* KO + Δ342); $p = 0.0007$ (TCTN3, *ADAMTS9* KO vs *ADAMTS9* KO + Δ342); $p = 0.0001$(CC2D2A, *Wt* vs *ADAMTS9* KO + Δ342); $p = 0.0004$(CC2D2A, *ADAMTS9* KO vs *ADAMTS9* KO + Δ342). Error bars indicate Mean ± S.D. **d** *TMEM67* patient variants and the underlying ciliopathies. **e**–**g** Ciliogenesis and cilium length of *TMEM67* KO cells transfected with patient variants. Yellow arrowheads indicate primary cilia, acetylated α-tubulin (green), γ-tubulin (red). $n = 100$ in (**f**) and $n = 90$ in (**g**), data from three independent experiments are shown. **** indicates a p-value <0.0001 in one-way ANOVA + Sidak's multiple comparison test for percentage ciliated cells and one-way Kruskal–Wallis test + Dunn's multiple comparison test for cilium length. Error bars indicate Mean ± S.D. **h** Western blot with commercial TMEM67 antibody (red) and GAPDH (green) of the conditioned medium (C.M.) and the cell lysates (C.L.) of *Wt* or *TMEM67* KO cells transfected with either empty vector (E.V.), Full-length, or the patient variants. Bar graphs represent quantifications from 3 independent experiments. **** indicates a p-value <0.0001, **<0.01, *<0.05 in one-way ANOVA + Sidak's multiple comparison test. $p = 0.0291$(*Wt* + EV vs *TMEM67* KO + EV); $p = 0.0076$(*TMEM67* KO + EV vs *TMEM67* KO + FL) in cell lysates. Error bars indicate Mean ± S.D. **i**, **j** TMEM67 commercial antibody (red) and CEP170 (green) immunostaining ($n = 30$ each group). Data from a single representative experiment from 3 independent experiments are shown (**j**). **** indicates a p-value <0.0001 in Kruskal–Wallis test + Dunn's multiple comparison test. Error bars indicate Mean ± S.D. **k** Mean pixel intensity of TZ proteins in *TMEM67* KO cells transfected with empty vector (E.V.), Full-length or patient variants. $n = 50$ cells in each group. Data from a single representative experiment from 3 independent experiments are shown. **** indicates a p-value <0.0001, ***<0.001, **<0.01 in two-way ANOVA. Error bars indicate Mean ± S.D. Scale bars in (**a**, **e**, **i**) are 10 μm and 500 nm in the (**a**) inset and 2 or 1 μm in (**e**, **i**) inserts.

the extracellular (TCTN1) and transmembrane components of the TZ (which forms the necklace) to the Y-linkers, which remain unaffected in both *TMEM67* KO and *ADAMTS9* KO TZs. We speculate that the TMEM67 CCD may act as a crucial molecular scaffold for its "outside-in" anchoring role at the TZ. A future study investigating a mutated CCD in TMEM67 Δ342 would provide valuable insight into answering this question. The mechanism leading to increased TZ localization of MKS1 and CEP290 observed in *ADAMTS9* KO cells is also currently unknown. It is possible that ADAMTS9-proteolytic activity may be indirectly regulating MKS1 and CEP290 protein levels via an unidentified intermediate substrate unrelated to TMEM67 cleavage. We did not investigate whether *MKS1* and *CEP290* transcription is upregulated in *ADAMTS9* KO cells either. Thirdly, since *ADAMTS9* KO cells are defective for ECM clearance, focal adhesion, and cell proliferation[31,33], it is possible that MKS1 and CEP290 protein levels may be regulated via these pathways, leading to their increased staining.

In addition to ciliary TZ assembly, here we have demonstrated that *Tmem67*$^{ΔCLE/ΔCLE}$ MEFs maintain their ability to phosphorylate ROR2, indicating that non-cleaved full-length TMEM67 maintains functionality in the non-canonical Wnt pathway. The in vivo data, in comparison to *Tmem67*-null brains, confirm that TMEM67 indeed performs two discrete functions and is involved in Wnt signaling regulation as well. The generation of the *Tmem67*$^{ΔCLE/ΔCLE}$ mouse model as part of this study provided a unique opportunity to investigate the dual functionality of TMEM67 reported in previous work by many others, which has been an unresolved and highly debated question in the field. Our study reveals that TMEM67 is not a *single functional protein* but is in fact *two functional isoforms* of a single gene product, acting in two distinct cellular compartments, and in two crucial cellular pathways simultaneously, and should be studied as such in the future. Whether the released N-terminal CRD fragment (N-331) retains its Wnt signaling activity is unknown. We hypothesize that the TMEM67 N-331 may retain its bioactivity and may function similarly to a soluble frizzled-related protein (SFRP)[57], and it may have the ability to augment both canonical and non-canonical Wnt signaling activity, acting long-range and non-cell autonomously. Future work probing this question will answer this aspect of TMEM67 cleavage uncovered by this work.

TMEM67 is the most commonly mutated gene in MKS, but is also causative of NPHP, JBTS, RHYNS, and COACH syndromes. The dual functionality of TMEM67, driven by proteolytic cleavage, may explain the huge range and severity of ciliopathies linked to *TMEM67* mutations, ranging from fetal lethality to adults with mild liver fibrosis. The N-terminal TMEM67 cleavage product identified here (TMEM67 N-331) and its potential use to augment dysregulated Wnt signaling in polycystic kidney disease and many other human diseases such as cancer, where altered Wnt signaling plays a central role[58–62], is an exciting new paradigm uncovered by this study, which we plan on exploring further in future studies.

Methods

Contact for reagent and resource sharing

Requests for resources, reagents, and further information should be directed to and will be fulfilled by the lead contact, Dr. Sumeda Nandadasa (Sumeda.Nandadasa@Umassmed.edu).

Mice

All mouse experiments conducted in this study were carried out under the IACUC-approved protocol (2021-0006). *Tmem67*$^{+/-}$ mice (C57BL/6NJ-*Tmem67*$^{em1(IMPC)J}$/Mmjax) generated by the KOMP were purchased from the Jackson Laboratory (JAX, 051248) and were maintained in the C57BL/6J background. *Tmem67*$^{ΔCLE/+}$ founder mice were generated in the C57BL/6J background by Cyagen (Santa Clara, CA) animal modeling service upon contract, as outlined in Supplementary Fig. 7a. In brief, targeted ES cell clones 2F7 and 1E-10 were injected into C57BL/6 albino embryos, which were then implanted into CD-1 pseudopregnant females. Founder animals were identified using coat color, and germline transmission was confirmed by breeding with C57BL/6J female mice and genotyping the resulting offspring. Two heterozygous male mice and two heterozygous female mice were generated from clones 1E-10 and 2F7, respectively, and were maintained as independent founder lines. PCR amplification and Sanger sequencing were used to verify the Neomycin cassette removal and correct mutagenesis of the target residues in both lines. Founder mice were bred for two additional generations with C57BL/6J male and female mice (JAX, 000664) prior to breeding heterozygous mice to generate homozygous *Tmem67*$^{ΔCLE/ΔCLE}$ mice.

Mammalian cell culture

Wild-type hTERT-RPE-1 (ATCC, CRL-4000) and CRISPR-Cas9 knockout cell lines for *TMEM67*[28] and *ADAMTS9*[31] were cultured in DMEM/F12 (Gibco;11330-032) with 10% FBS and 200 U/mL penicillin/streptomycin (Gibco; 15140-122) and maintained at 37 °C with 5% CO_2. RPE-1 growth medium was supplemented with 0.01 mg/mL hygromycin B (Invitrogen; 10687010). Mouse embryonic fibroblasts were harvested from E13.5 embryos from timed mating and cultured for one week in DMEM/F12 medium containing 10% FBS and 200 U/mL penicillin/

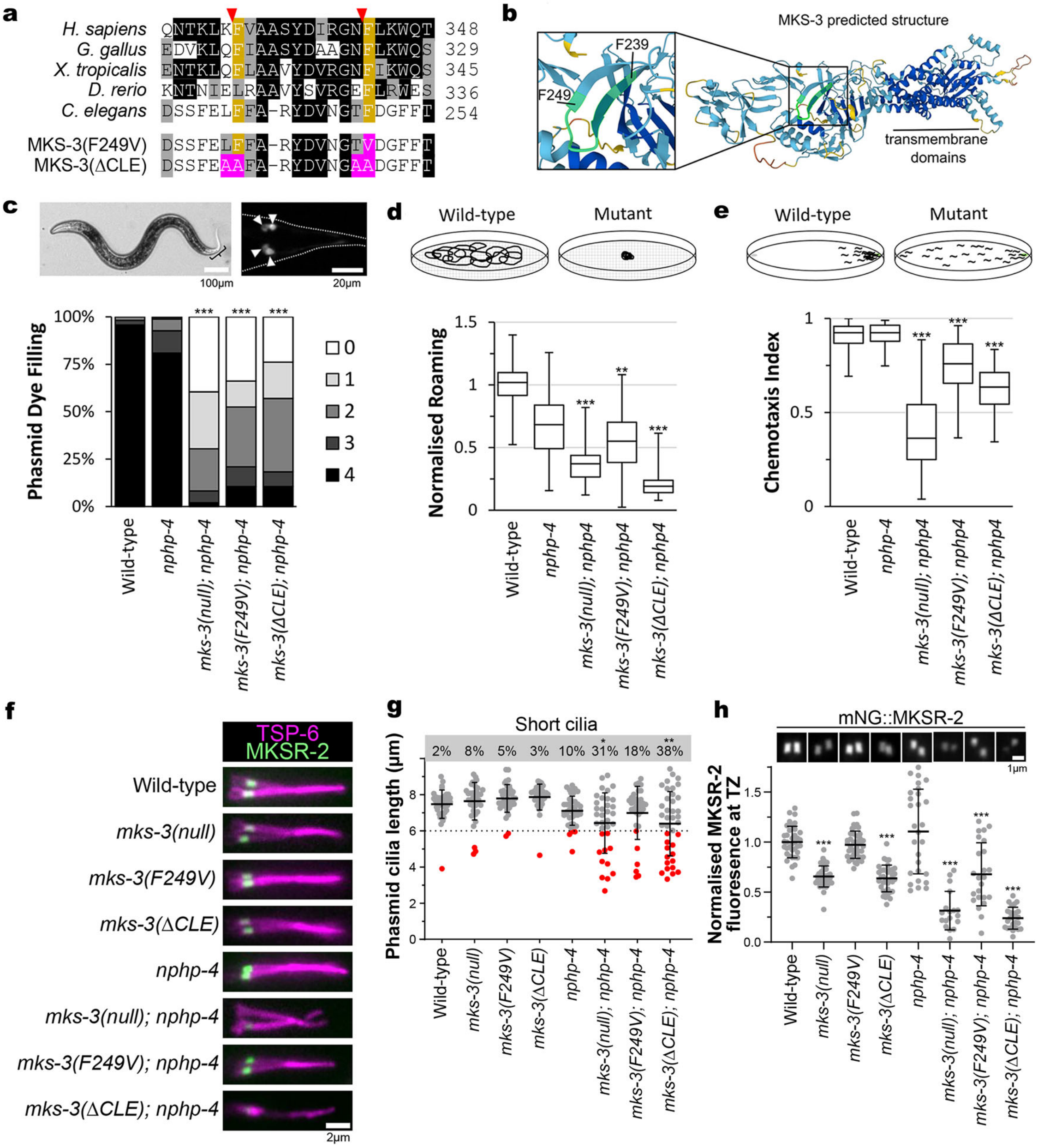

Fig. 5 | TMEM67 cleavage residues are essential for *C. elegans* MKS-3 function. **a** Alignment of TMEM67 cleavage sites. Identical(black), similar(gray), cleavage/phenylalanine(yellow), and mutated(magenta) residues are highlighted. **b** AlphaFold model of *C. elegans* MKS-3(AF-Q20046-F1) with predicted cleavage sites(green). Backbone indicates AlphaFold confidence score (blue = high to orange = low). **c** Assessment of cilium integrity with dye uptake by four ciliated neurons (arrowheads). Three biological replicates were performed with the following sample sizes and *p*-values: Wild-type *n* = 258, *nphp-4 n* = 246, *mks-3(null); nphp-4 n* = 243($p < 1E-10$), *mks-3(F249V); nphp-4 n* = 124($p < 1E-10$), and *mks-3(ΔCLE); nphp-4 n* = 142($p < 1E-10$). Statistical significance calculated with Kruskal–Wallis and Dunn's post hoc test. **d** Assessment of sensory cilium function with foraging behavior. Three biological replicates were performed with the following sample sizes and *p*-values: Wild-type *n* = 86, *nphp-4 n* = 86, *mks-3(null); nphp-4 n* = 85($p < 1E-10$), *mks-3(F249V); nphp-4 n* = 42($p = 0.0028$), and *mks-3(ΔCLE); nphp-4 n* = 45($p < 1E-10$). Box plots indicate the maximum/minimum(bars), median, lower, and upper quartiles. Statistical significance was calculated with one-way ANOVA and post hoc Tukey test. **e** Assessment of sensory cilium function using chemotaxis towards benzaldehyde. Three biological replicates were performed with the following sample sizes and *p*-values: Wild-type *n* = 49, *nphp-4 n* = 50, *mks-3(null); nphp-4 n* = 50($p < 1E-10$), *mks-3(F249V); nphp-4 n* = 24($p = 2.3E-6$), and *mks-3(ΔCLE); nphp-4 n* = 27($p < 1E-10$). Box plots indicate the maximum/minimum(bars), median, lower, and upper quartiles. Statistical significance was calculated with one-way ANOVA and post hoc Tukey test. **f**, **g** Cilia length assessed with TSP-6::mScarlet(magenta) that localizes to the ciliary/periciliary membranes. Short cilia are defined as <6 µm(red dots), and incidence is indicated. Three biological replicates were performed. Error bars indicate Mean ± S.D. Sample sizes and *p*-values: Wild-type *n* = 43, *mks-3(null) n* = 39($p = 0.3423$), *mks-3(F249V) n* = 38($p = 0.5978$), *mks-3(ΔCLE) n* = 34($p > 0.9999$), *nphp-4 n* = 42, *mks-3(null); nphp-4 n* = 35($p = 0.0212$), *mks-3(F249V); nphp-4 n* = 33($p = 0.3199$), and *mks-3(ΔCLE); nphp-4 n* = 39($p = 0.0033$). Statistical significance calculated using two-sided Fisher's Exact test. **h** Quantification of mNeonGreen::MKSR-2. Three biological replicates were performed. Error bars indicate Mean ± S.D. Sample sizes and *p*-values: Wild-type *n* = 37, *mks-3(null) n* = 40($p = 3E-10$), *mks-3(F249V) n* = 41($p = 0.9992$), *mks-3(ΔCLE) n* = 36($p < 1E-10$), *nphp-4 n* = 28, *mks-3(null); nphp-4 n* = 18($p < 1E-10$), *mks-3(F249V); nphp-4 n* = 24($p = 1E-10$), and *mks-3(ΔCLE); nphp-4 n* = 24($p < 1E-10$). Statistical significance was calculated with one-way ANOVA and post hoc Tukey test. In all panels *** indicate a *p*-value <0.001, **<0.01, *<0.05. Scale bars in (**c**) are 100 µm and 20 µm, 2 µm in (**f**), and 1 µm in (**h**).

streptomycin and passaged once prior to immortalization with Simian virus 40 large T antigen (SV40LT), as previously described[63].

Plasmid DNA constructs and transfections

The TMEM67 cleavage site mutations (S1, S2, and S1 + S2) and ciliopathy patient variants (F343V, K329T, and L349S) were generated using the Q5 Site-Directed Mutagenesis Kit (NEB; E0554S) utilizing the full-length, human TMEM67 plasmid construct in the pCDNA3.1Myc/His vector backbone, originally cloned by the Johnson lab[28]. TMEM67 Δ342 and N-331 constructs were cloned into the HindIII(5′) and XhoI(3′) restriction enzyme sites of the pSecTag2C vector (Invitrogen, V900-20) following overhang PCR amplification of the human Fl-TMEM67-Myc construct using Phusion High-Fidelity Taq DNA Polymerase (NEB, M0530). Both constructs were cloned in frame to the N-terminal Ig κ-

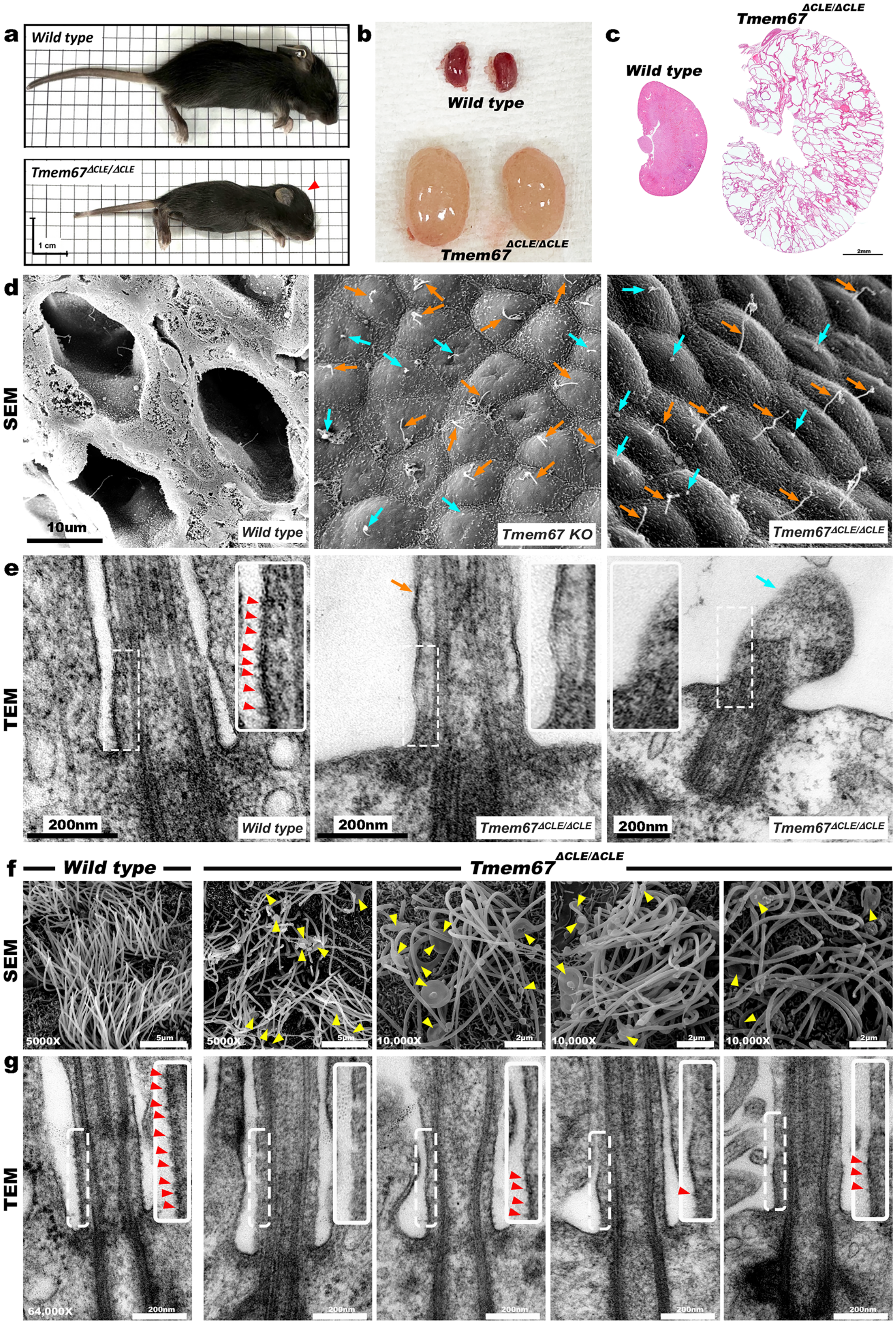

Fig. 6 | Characterization of a *Tmem67*$^{\Delta CLE/\Delta CLE}$ mouse model reveals that loss of TMEM67 cleavage leads to ciliopathy formation in mammals. a *Wt* and *Tmem67*$^{\Delta CLE/\Delta CLE}$ littermates at postnatal day 14 (p14) showing impaired growth and a dome-shaped head (red arrowhead) indicative of hydrocephalus formation in *Tmem67*$^{\Delta CLE/\Delta CLE}$ mice (*n* = 10/10 mice). **b** Kidneys dissected from *Wt* and *Tmem67*$^{\Delta CLE/\Delta CLE}$ littermates at p14 showing highly enlarged polycystic kidneys in the mutant mice (*n* = 10/10 mice). **c** Hematoxylin and Eosin stained kidney sections from p14 mice show highly cystic renal histopathology in the *Tmem67*$^{\Delta CLE/\Delta CLE}$ mutant kidneys compared to that of a *Wt* littermate. *n* = 3 kidneys from each group. **d** Freeze-fracture scanning electron microscopy (SEM) shows defective primary cilia formation in *Tmem67*$^{\Delta CLE/\Delta CLE}$ kidneys, similar to *Tmem67* KO kidneys. The turquoise arrows indicate short cilia, and orange arrows indicate extended primary cilia with abnormal morphologies present on *Tmem67* KO and *Tmem67*$^{\Delta CLE/\Delta CLE}$ cystic renal tubular epithelium (*n* = 3 kidneys from each group). **e** Transmission electron microscopy (TEM) images of primary cilia showing the transition zone "necklace" (red arrowheads) in a *Wt* cilium are entirely missing in both types of *Tmem67*$^{\Delta CLE/\Delta CLE}$ primary cilia. The turquoise and orange arrows indicate a short or an extended primary cilium section visualized by TEM (*n* = 3 kidneys from each group). **f** SEM images showing highly abnormal, tangled motile cilia with large membrane-bulges (yellow arrowheads) and bulbus-tips present in the ependymal cells lining the lateral brain ventricles in *Tmem67*$^{\Delta CLE/\Delta CLE}$ mice compared to the uniformly organized motile cilia seen in the *Wt* brain ventricles (*n* = 3 brains from each group). **g** TEM images show a similar loss of the TZ necklace formation (red arrowheads) in the *Tmem67*$^{\Delta CLE/\Delta CLE}$ motile ependymal cilia in comparison to *Wt* (*n* = 3 brains from each group). Scale bar in (**a**) is 1 cm, 2 mm in (**c**), 10 μm in (**d**), 5 μm or 2 μm in (**f**), and 200 nm in (**e** and **g**).

chain leader sequence (vector signal peptide) and the 6× His and Myc tag at the C-terminus. The TMEM67 endogenous signal peptide sequence (M^1-A^{36}) was not PCR amplified in generating the N-331 construct to prevent duplication of signal peptides and coded only for TMEM67 Q^{37}-K^{331}, while the TMEM67 Δ342 construct coded for F^{343}-F^{993} of human TMEM67. Ligated DNA was transformed into DH5α competent *E. coli* (NEB; C2987H) and grown on LB plates containing 100 μg/mL carbenicillin. Plasmid DNA was extracted with the ZymoPURE II plasmid midiprep kit (Zymo Research; D4200). All constructs were sequence verified to be free of any undesired mutations by Sanger sequencing. Plasmid DNA transfections were carried out using the PEI MAX transfection reagent (Polysciences; 24765) diluted in Opti-MEM reduced serum medium (Gibco; 31985-070). 300 ng of DNA was transfected per well into 8-chamber slides (Corning; 354118) or 1.5 μg per well in 6-well plates. Transfected cells were incubated at 37 °C, 5% CO_2 for 6 h or overnight.

Immunostaining and fluorescence microscopy of cultured cells

For immunostaining analysis, RPE-1 or MEF cells were cultured in 8-well chamber slides in DMEM/F12 medium containing 10% FBS, followed by serum starvation for 24 h to induce ciliogenesis. For visualizing primary cilia, samples were fixed in fresh 4% paraformaldehyde in 0.1% PBS-Tween (PBST) at room temperature (RT) for 20 min. For immunolabelling of the transition zone markers, cells were washed once in PBS and fixed in ice-cold methanol for 5 min at −20 °C. The fixed cells were washed three times in PBST and blocked in 5% normal goat serum made in PBST for 1 h at RT. Primary and secondary antibodies were diluted in 5% normal goat serum in PBST. Antibodies and dilutions used are listed in Supplementary Table 5. Samples were incubated with primary antibodies at 4 °C overnight and secondary antibodies for 2 h at RT, followed by 3 × 10 min washes with PBST and mounted with Prolong gold mounting media with DAPI (Invitrogen, P36931). For non-permeable cell surface labeling of TMEM67 N and Alexa-488 conjugated wheat germ agglutinin (WGA), cells cultured in 8-chamber slides were fixed in 4% PFA made in PBS for 20 min and washed 3× with PBS. Cells were blocked in 5% NGS made in PBS for 1 h and incubated in primary antibody and WGA overnight. Cells were washed 3× with PBS and incubated with secondary antibody at RT for 2 h. Following 3× washes in PBS, cells were mounted with Prolong gold mounting media with DAPI. Confocal images were acquired using a Leica SP8 laser scanning confocal microscope with a ×63 1.47 NA oil-immersion objective, utilizing the HyD hybrid detectors. The SP8 lightning feature was used for super-resolution images of the transition zone collected at a 1000× magnification.

Fluorescence microscopy quantifications and statistical analysis

Measurements of cilia length/frequency and intensity of the ciliary transition zone were quantified using NIH Image J (FIJI). Cell counter and line trace functions were used for measuring the percentage of ciliated cells and cilium lengths. Pixel intensity of the transition zone markers was quantified by measuring the mean pixel intensity of an ROI and performing background subtraction. In brief, a boxed region of interest (ROI) was drawn directly above the CEP170 staining and transferred to the corresponding transition zone marker channel (red/568 channel), and the arbitrary mean pixel intensity for the ROI was measured. The "restore selection" function was used to transfer the same ROI to all transition zones analyzed. GraphPad Prism 10 software (La Jolla, CA) was used to determine statistical significance by the indicated statistical tests in the figure legends.

Transmission and Scanning Electron Microscopy

Mouse brains and kidneys were dissected and immediately fixed in 2.5% glutaraldehyde with 1.6% paraformaldehyde in 0.1 M sodium cacodylate buffer (pH 7.2). Samples were processed and analyzed at the University of Massachusetts Chan Medical School Electron Microscopy core facility according to standard procedures. Briefly, fixed samples were moved into fresh 2.5% glutaraldehyde, 1.6% paraformaldehyde in 0.1 M sodium cacodylate buffer and left overnight at 4 °C. The samples were then rinsed twice in the same fixation buffer and post-fixed with 1% osmium tetroxide for 1 h at room temperature. Samples were washed twice with DH_2O for 5 min and then dehydrated through a graded ethanol series of 20% increments and two changes in 100% ethanol. Samples were then infiltrated with two changes of 100% propylene oxide first and then with a propylene oxide and SPI-Pon 812 50%–50% resin mixture overnight. Three changes of fresh 100% SPI-Pon 812 resin were done before the samples were polymerized at 68 °C in plastic capsules. Samples were oriented, and 70 nm ultra-thin sections were collected using a Leica EM UC7 ultramicrotome equipped with a Diatome ultra 45 diamond knife. Sections were placed on copper support grids and contrasted with lead citrate and uranyl acetate. Sections were examined using a FEI Tecnai 12 BT with 120 kV accelerating voltage, and images were captured using a Gatan TEM CCD camera. Samples processed for SEM and bulk-frozen-fracture SEM (kidneys) were fixed as above, then dehydrated through a graded series of ethanol and either directly critical point dried or quickly immersed in liquid nitrogen, placed on a liquid nitrogen-cooled block, and fractured. The tissue pieces were thawed in 100% ethanol and critical point dried. The samples were then mounted on aluminum SEM stubs and metal-coated (Au/Pb, 60/40) and imaged on a FEI Quanta 200 MKII FeSEM.

Western blotting

Cells cultured in 6-well plates were lysed using 500 μl Transmembrane lysis buffer (FIVEphoton Biochemicals; TmPER-50) for TMEM67 detection, or ice-cold Pierce RIPA lysis buffer (Thermo Fisher; 8901) for ROR2 detection. Lysis buffer was supplemented with Pierce protease inhibitor complex with EDTA (Thermo Fisher; A32953) and Pierce phosphatase inhibitor (Thermo Fisher; A32957). For serum-free conditioned medium analysis of *Wild-type* and *ADAMTS9* KO RPE-1 cells, cells were grown to confluency in 10 cm tissue culture plates, and conditioned medium was collected for 72 h after two PBS washes. For conditioned medium collection of transient transfected experiments

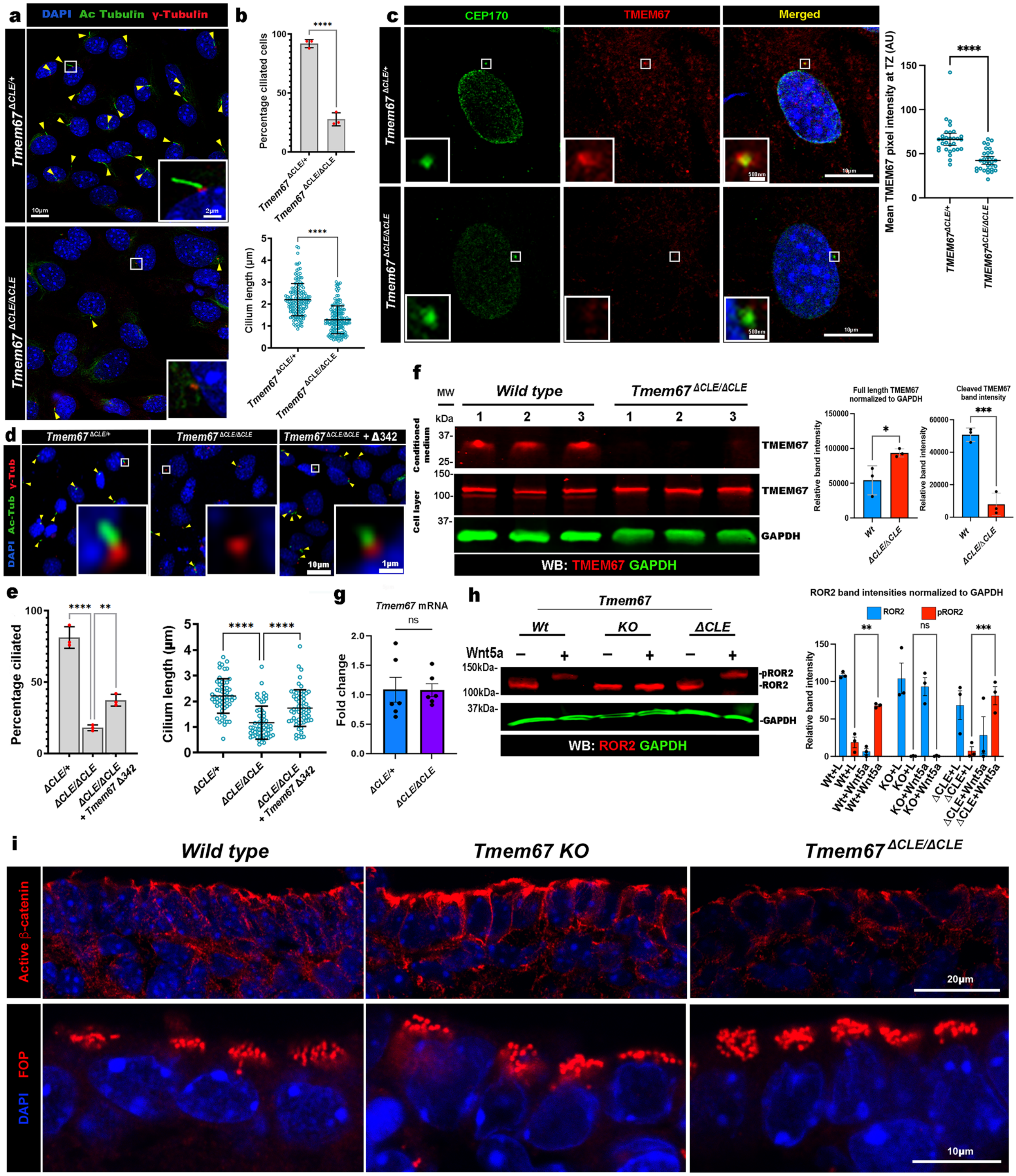

carried out in 6-well plates, serum-free medium was collected for 24 h post-transfection after a single PBS wash step. 6× Laemmli sample buffer containing 9% 2-mercaptoethanol, 4.8% glycerol, 6% SDS, and 0.03% bromophenol blue was used for boiling cell lysates or conditioned medium samples for 10 min at 100 °C prior to SDS-PAGE analysis. 6% acrylamide gels electrophoresed for 2.5 h at 60 V were used for ROR2 phosphorylation band shift detection upon Wnt5a treatment, and 7.5% acrylamide gels were used in all other experiments. Proteins were transferred to Immobilon-FL transfer membranes (EMD Millipore; IPFL00010) and blocked with 5% nonfat dry milk in 0.1% PBS-Tween for 1 h. Experiments detecting ROR2 used LI-COR Intercept blocking buffer (Li-COR; 927-620001) for blocking and primary antibody incubation. In all other experiments, primary and secondary antibodies were diluted in 5% nonfat dry milk in 0.1% PBS-Tween. Primary antibodies were diluted 1:1000 and incubated at 4 °C overnight. LI-COR secondary antibodies (LI-COR Biosciences, Lincoln, NE) were diluted 1:10,000 and incubated for 2 h at room temperature. A complete list of all antibodies and dilutions used is provided in the Supplementary Table 5. A LI-COR Odyssey M scanner was used to image fluorescent western blot membranes.

Fig. 7 | Loss of ciliogenesis but normal Wnt signaling in *Tmem67*$^{\Delta CLE/\Delta CLE}$ embryonic fibroblasts and brains. a, **b** *Tmem67*$^{\Delta CLE/\Delta CLE}$ mouse embryonic fibroblasts (MEFs) show significantly shorter and fewer primary cilia (yellow arrowheads) marked by acetylated α-tubulin (green) and γ-tubulin (red). Data from 3 independent experiments are shown. **** indicates a p-value <0.0001 in a two-tailed unpaired t-test for percentage ciliated cells ($n = 100$) and Mann–Whitney test for cilium length ($n = 150$). Error bars indicate Mean ± S.D. **c** CEP170 (green) and TMEM67 (red) immunostaining of MEFs. Data from one representative experiment from 3 independent experiments are shown ($n = 30$ for each group per experiment). **** indicates a p-value <0.0001 in a two-tailed Mann–Whitney test. Error bars indicate Mean ± S.D. **d**, **e** Transfection of *Tmem67*$^{\Delta CLE/\Delta CLE}$ MEFs with TMEM67 Δ342 significantly improves ciliogenesis ($n = 100$) and cilium length ($n = 60$). $n = 3$ independent experiments. **** indicates p-value <0.0001, **<0.01 in Kruskal–Wallis test + Dunn's multiple comparison test for cilium length and one-way ANOVA with a Sidak's multiple comparison test for percentage ciliated cells. $p = 0.0072$ (ΔCLE/ΔCLE vs ΔCLE/ΔCLE + Δ342). Error bars indicate Mean ± S.D. **f** Western blotting with TMEM67 commercial antibody (red) and GAPDH (green) from *Wt* and *Tmem67*$^{\Delta CLE/\Delta CLE}$ MEF conditioned medium and cell layers from triplicate biological replicates. *** indicates p-value <0.001($p = 0.0008$), *<0.05($p = 0.0348$) in two-tailed unpaired t-test. Error bars indicate Mean ± S.D. **g** qRT-PCR of *Tmem67*$^{\Delta CLE/+}$ and *Tmem67*$^{\Delta CLE/\Delta CLE}$ MEFs. Data represent triplicate biological replicate cultures run with duplicate PCR reactions. $p = 0.9756$(ns) in two-tailed unpaired t-test. Error bars indicate Mean ± S.E.M. **h** Western blot showing ROR2 (red) phosphorylation is unaffected in *Tmem67*$^{\Delta CLE/\Delta CLE}$ MEFs in response to Wnt5a treatment, whereas *Tmem67-null* MEFs do not respond to Wnt5a treatment. ROR2 band intensities from 3 independent experiments are shown. *** indicates a p-value <0.001($p = 0.0002$), **<0.001($p = 0.0092$) in two-way ANOVA with a Sidak's multiple comparison test. Error bars indicate Mean ± S.E.M. **i** Active β-catenin or FOP immunostaining (red) of *Wt*, *Tmem67 KO*, and *Tmem67*$^{\Delta CLE/\Delta CLE}$ lateral brain ventricles ($n = 3$ brains from each group). Scale bars in (**a**) are 10 μm and 2 μm, and 10 μm in (**c**), 5 μm in (**d**), 20 μm and 10 μm in (**i**).

qRT-PCR

RNA was harvested from RPE-1 cells or MEFs cultured in 6-well culture plates or using whole mouse kidneys. Briefly, mRNA was harvested by lysing cells with 300 μl or 500 μl for minced whole kidneys in Trizol reagent and snap freezing in liquid nitrogen. Thawed samples were sonicated for 30 s followed by chloroform extraction and isopropanol precipitation. RNA pellets were washed with 70% ethanol and dissolved in ultra-pure ddH_2O. 2 μg of mRNA from each sample was used in cDNA synthesis using the High-Capacity cDNA Reverse Transcription Kit (Thermo Fisher; 4368814). A BioRad CFX connect real-time PCR machine was used in combination with Bullseye EvaGreen qPCR master mix (Midsci; BEQPCR-R) for determining ΔCT values. qRT-PCR primers used in this study are provided in Supplementary Table 1. *Gapdh, β-Actin*, or *18s* ribosomal RNA expression was used for normalizing samples. Each sample was run in duplicate with at least 3 experimental/biological replicates per group. Fold change was quantified by determining the 2^(-ΔΔCT) values in relation to the average expression value of the control group. Unpaired Student's two-tailed t-tests were used to assess statistical significance, and GraphPad Prism (version 10.3.0) was used to generate bar graphs.

Tissue histopathology and immunostaining analysis

For Haematoxylin and Eosin (H&E) staining, dissected kidney, heart, and liver samples were fixed in 4% PFA made in PBST at 4 °C overnight, washed three times in PBST, and paraffin-embedded using a standard tissue processing procedure. 7 μm paraffin sections were collected using a Leica RM2155 motorized microtome, deparaffined and stained with Haematoxylin and Eosin, and mounted in Cystoseal XYL medium (Adwin Scientific; NC9527349). For Masson's Trichrome staining of livers, paraffin sections were deparaffined, refixed in Bouin's fixative (Electron Microscopy Sciences (EMS); 26367-01) for 1 h at 56 °C, stained with Weigert's iron Haematoxylin A & B solutions (EMS; 26367-02 and -03), Biebrich scarlet solution (EMS; 26367-04), and Aniline blue (EMS; 26367-06) solutions and treated with acetic acid prior to mounting in Cytoseal XYL mounting medium. For immunostaining brain sections, dissected mouse brains were fixed overnight at 4 °C in 4% PFA made in PBST, washed three times in PBS, and consecutively dehydrated in 15% sucrose and 30% sucrose overnight at 4 °C. Samples were cryo-embedded in OCT (Tissue-Tek; 4583), and 7 μm cryo sections were collected using a Leica CM 1950 cryostat at −25 °C. Thawed cryo sections were washed in PBS, blocked for 1 h in 5% normal goat serum in PBST at room temperature, and stained with primary antibodies overnight at 4 °C, diluted in 5% normal goat serum in PBST. A complete list of all antibodies and dilutions used is provided in the Supplementary Table 5. Sections were washed thrice in PBST and incubated with secondary antibodies diluted in PBST for 2 h at room temperature. Sections were washed thrice in PBST and sealed overnight in Prolong gold antifade mounting medium with DAPI (Invitrogen, P36931). A Leica SP8 confocal microscope was used for imaging brain sections, and a TissueGnostics-SL slide scanner was used for imaging kidney and heart H&E-stained sections. Liver H&E and Masson's trichrome stained sections were imaged using a Zeiss Axioplan widefield microscope equipped with a Leica DMC6200 color camera.

Caenorhabditis elegans strains and maintenance

C. elegans worm strains were maintained at 20 °C on NGM agar plates seeded with OP50 *E. coli* using standard husbandry techniques[64]. A list of worm strains generated and/or used in this study is in Supplementary Table 2.

CRISPR/Cas9 genome engineering in *C. elegans*

The F249V and ΔCLE (L^{238}-A, F^{239}-A, T^{248}-A, F^{249}-A) CRISPR mutants were generated by injecting the Cas9 ribonucleoprotein complex[65] into *nphp-4(tm925)* worms. Edited progeny were identified using an *unc-58* co-CRISPR strategy[66], and *unc-58* was sequenced in all CRISPR strains to ensure it was wild-type[67]. Worms that contained the engineered edit were identified using a PCR-based approach[28]. *C. elegans* primers used in this study are in Supplementary Table 3. Single-stranded oligonucleotides (Sigma) were used as repair templates to engineer precise edits. CRISPR reagents were purchased from IDT: Alt-R Cas9 Nuclease V3 (IDT; 1081058), Alt-R tracrRNA (IDT; 1072533), and custom-generated, gene-specific Alt-R crRNA. crRNA and repair template sequences are listed in Supplementary Table 4. All CRISPR mutants were confirmed by Sanger sequencing and outcrossed twice before analysis.

C. elegans quantitative assays to assess cilia structure/function

Dye filling assays were performed with DiO (Invitrogen; D275) diluted in M9 (22 mM KH_2PO_4, 42 mM Na_2HPO_4, 85.5 mM NaCl, 1 mM $MgSO_4$). Synchronized populations of young adult hermaphrodites were incubated for 1 h with 10 ng/μl DiO solution, then allowed to recover on NGM plates for 30 min before being mounted on 4% agarose pads with 40 mM tetramisole (Sigma; L9756). Worms were visualized with a 20× objective on a Leica DM5000B epifluorescence microscope. Dye filling was quantified by counting the number of phasmid neurons with dye uptake. The sample size was more than 120 worms from at least three independent replicates. Roaming assays were performed by placing a single hermaphrodite on a fully seeded NGM plate for 20 h at 20 °C. The worm was removed from the plate, and a 5 mm^2 grid was placed under it to count how many squares the worm entered. All values were normalized to *wild type* (sample size at least 40 worms from three independent replicates). Chemotaxis plates (9 cm petri dishes with 10 ml of chemotaxis agar: 2% agar, 5 mM KPO_4 pH 6, 1 mM $CaCl_2$, 1 mM $MgSO_4$) were prepared

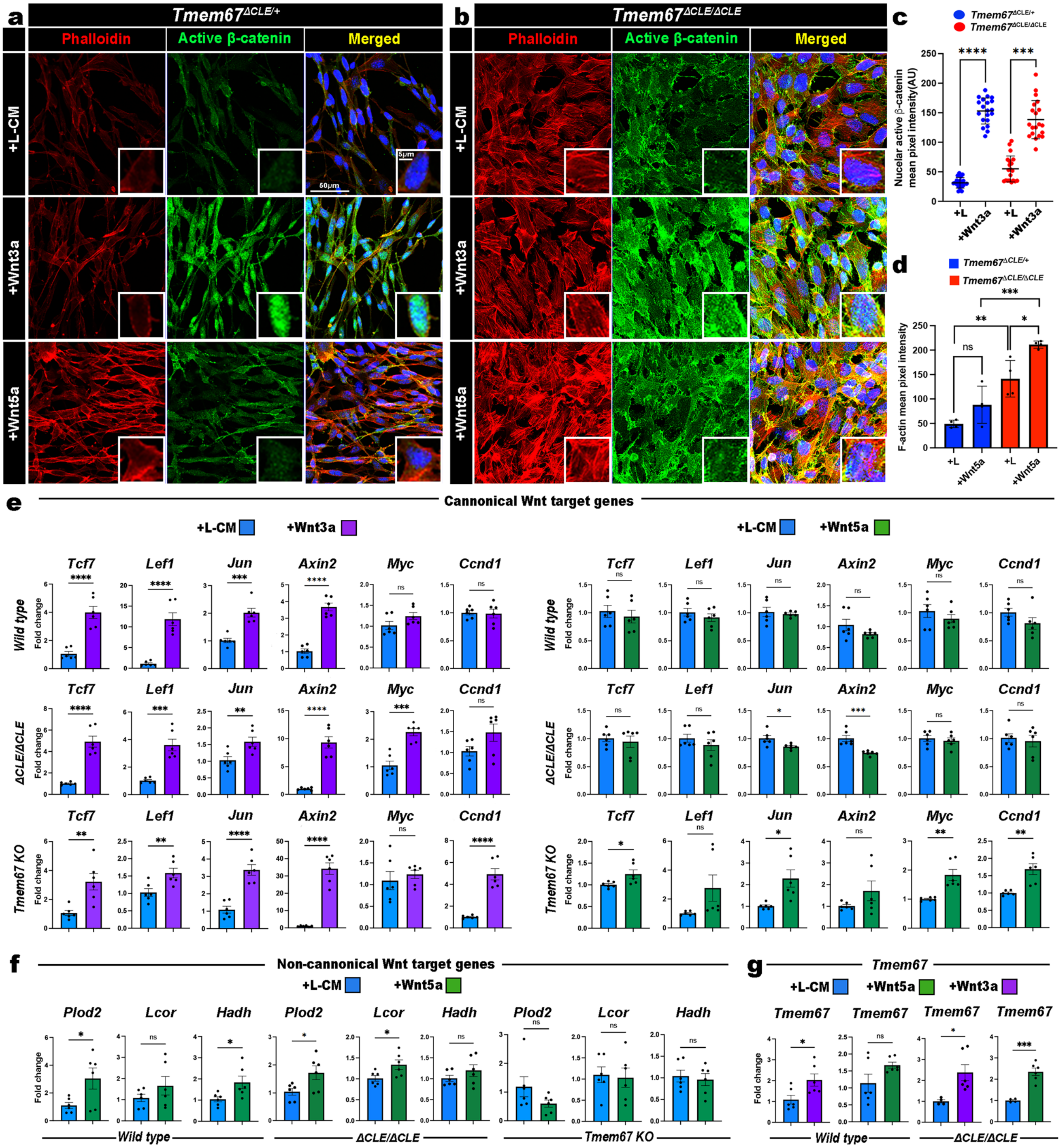

Fig. 8 | $Tmem67^{\Delta CLE/\Delta CLE}$ MEFs respond to canonical and non-canonical Wnt signaling. a–d $Tmem67^{\Delta CLE/+}$ and $Tmem67^{\Delta CLE/\Delta CLE}$ MEFs stained for active β-catenin (green) and F-actin (Phalloidin, red) upon L-cell (control), Wnt3a, and Wnt5a conditioned medium treatment. Mean nuclear active β-catenin signal from 20 nuclei from each group is shown ($n = 3$ independent experiments), **** indicates a p-value <0.0001, ***<0.001 ($p = 0.0002$) in one-way Kruskal–Wallis test with a Dunn's multiple comparison test in (**c**). Mean F-actin pixel intensity from 4 different fields of cells in each group is shown in (**d**) ($n = 4$ independent experiments), *** indicates a p-value <0.001($p = 0.0002$), **<0.01($p = 0.0021$), *<0.05($p = 0.0158$) in a one-way ANOVA with Tukey's multiple comparisons test. Error bars indicate Mean ± S.D. in (**c** and **d**). **e** qRT-PCR for indicated genes in *Wt*, $Tmem67^{\Delta CLE/\Delta CLE}$, and *Tmem67-null* MEFs treated with L-cell (blue), Wnt3A (purple), or Wnt5a (green) conditioned medium. **** indicates a p-value <0.0001, ***<0.001, **<0.01, *<0.05 in two-tailed unpaired t-test. Error bars indicate Mean ± S.E.M. Data represent 3 independent experiments. $p = 0.0002$(*Jun*, *Wt*+Wnt3a), $p = 0.1135$(*Myc*, *Wt*+Wnt3a), $p = 0.8644$(*Ccnd1*, *Wt*+Wnt3a), $p = 0.0001$(*Lef1*, *ΔCLE*+Wnt3a), $p = 0.0099$(*Jun*, *ΔCLE* +Wnt3a), $p = 0.0002$(*Myc*, ΔCLE+Wnt3a), $p = 0.6816$(*Ccnd1*, *ΔCLE*+Wnt3a), $p = 0.0045$(*Tcf7*, *KO*+Wnt3a), $p = 0.0099$(*Lef1*, *KO*+Wnt3a), $p = 0.5507$(*Myc*, *KO* +Wnt3a), $p = 0.0241$(*Jun*, *ΔCLE*+Wnt5a), $p = 0.0009$(*Axin2*, *ΔCLE*+Wnt5a), $p = 0.0323$(*Tcf7*, *KO*+Wnt5a), $p = 0.0101$(*Jun*, *KO*+Wnt5a), $p = 0.0013$(*Myc*, *KO* +Wnt5a), $p = 0.0016$(*Ccnd1*, *KO*+Wnt5a). **f** qRT-PCR for indicated genes in *Wt*, $Tmem67^{\Delta CLE/\Delta CLE}$ and *Tmem67-null* MEFs treated with L-cell (blue) or Wnt5A (green) medium * indicates a p-value <0.05 in two-tailed unpaired t-test. Error bars indicate Mean ± S.E.M. Data represent 3 independent experiments. $p = 0.0337$(*Plod2*, *Wt* +Wnt5a), $p = 0.0311$(*Hadh*, *Wt*+Wnt5a), $p = 0.0328$(*Plod2*, *ΔCLE*+Wnt5a), $p = 0.0321$(*Lcor*, *ΔCLE*+Wnt5a). **g** qRT-PCR for *Tmem67* in *Wt* and $Tmem67^{\Delta CLE/\Delta CLE}$ MEFs treated with Wnt5A (green) or Wnt3A (purple). *** indicates a p-value <0.001, *<0.05 in in two-tailed unpaired t-test. Error bars indicate Mean ± S.E.M. Data represent 3 independent experiments. $p = 0.0262$(*Wt*+Wnt3a), $p = 0.0227$(*ΔCLE* +Wnt3a), $p = 0.0003$ (*ΔCLE*+Wnt5a). Scale bars in (**a**) are 50 μm and 5 μm.

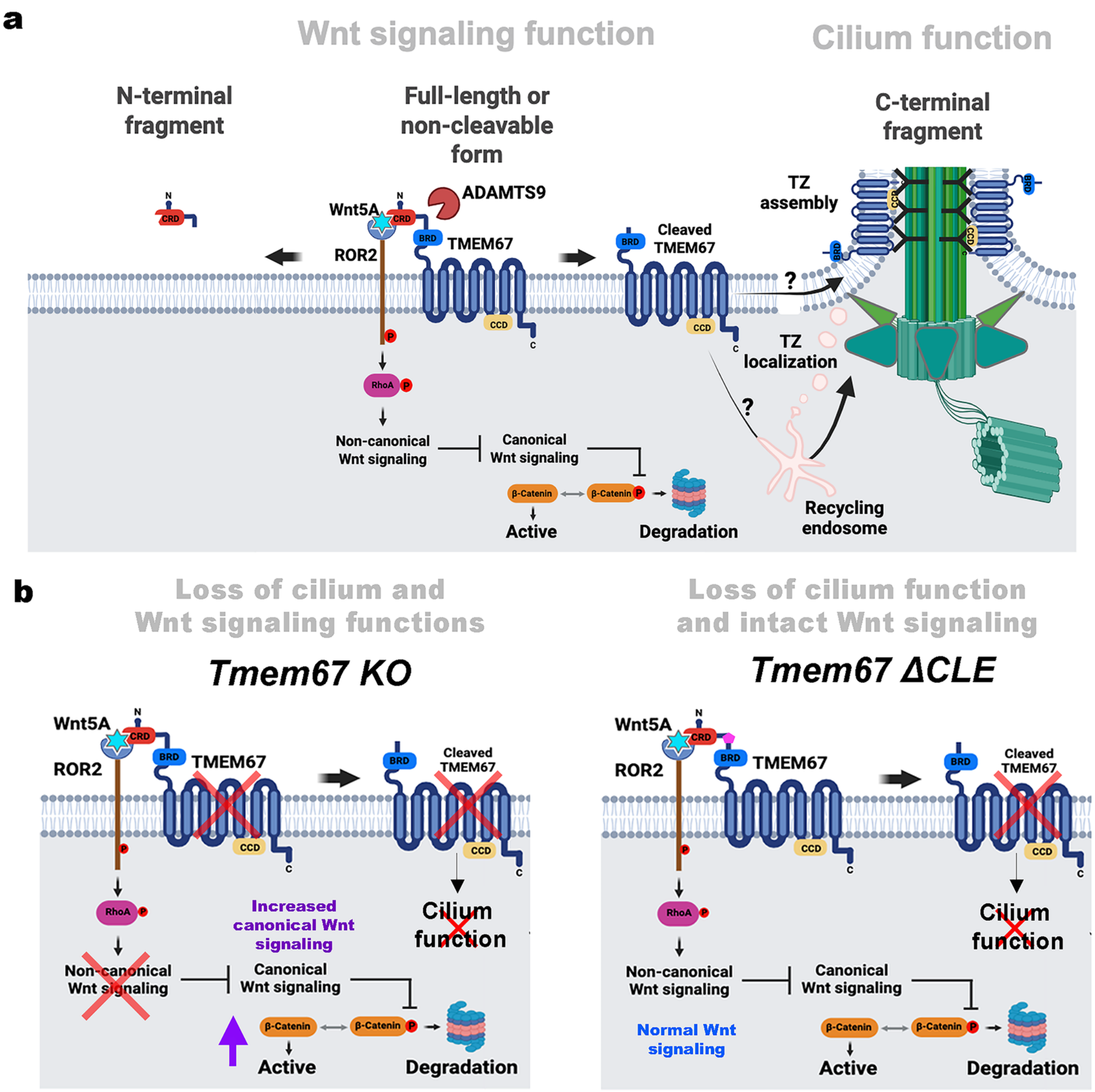

Fig. 9 | Model of the two functional forms of TMEM67 regulating Wnt signaling and transition zone assembly in *Tmem67*-null and *Tmem67*$^{\Delta CLE/\Delta CLE}$ mouse models. a Cartoon depicting the proposed new model of how ADAMTS9-mediated TMEM67 cleavage regulates the abundance of two functional forms of TMEM67, which are active in two distinct cell membrane compartments. The N-terminally trimmed (TMEM67 Δ342) form localizes to the ciliary transition zone and regulates transition zone assembly, while the full-length form acts to regulate normal Wnt signaling on the cell surface. **b** Cartoon depicting the loss of both Wnt signaling and cilium functions in the *Tmem67* KO, while *Tmem67*$^{\Delta CLE/\Delta CLE}$ mice transduce normal Wnt signaling but lose the ciliary TZ function. Created in BioRender. Nandadasa, H. (2025) https://BioRender.com/5kxulbe.

16–24 h before the experiment. Two spots were marked on opposite sides of the plates, 1.5 cm from the edge, and 1 µl of 1 M sodium azide (Sigma; S2002) was added to each spot. 1 µl of ethanol (Honeywell; 32294) or 1:200 benzaldehyde (Sigma; B1334) diluted in ethanol was then added to the spots. Young adult hermaphrodites were washed and added to the center of the plate. Excess liquid was removed, and the worms were counted after 1 h. The chemotaxis index was calculated as $(b-c)/n$, where b is the number of worms within 1.5 cm of the benzaldehyde spot, c is the number of worms within 1.5 cm of the ethanol control, and n is the total number of worms on the plate. Three independent replicates were performed, with at least 24 assays performed for each genotype.

Fluorescent imaging to assess transition zone and cilia integrity in *C. elegans*

Generation and validation of *mksr-2(oq108[mNeonGreen::MKSR-2])*[68] and *tsp-6(syb4122[TSP-6::mScarlet])*[69] endogenously tagged proteins have been previously described. Standard genetic crossing techniques were used to introduce the fluorescent proteins into the *mks-3* and *nphp-4* mutants, and strains were confirmed by PCR. All *C. elegans* genotyping primers used in this study are listed in the Supplementary Table 3. All images were acquired on an upright Leica DM5000B epifluorescence microscope with a 100× oil-immersion objective and captured with an Andor iXon + camera run by Andor software. All image analysis and preparation were performed with Image J. For imaging experiments, all data were acquired in at least 3 biological replicates with a final sample size greater than or equal to 18. For two-color images, channels were manually aligned to account for the drift of the samples. mNG::MKSR-2 levels at the transition zone were quantified as previously described[68]. Phasmid cilia length was determined by using a segmented line to measure the length of the TSP-6::mScarlet signal from a maximum projection of the entire length of the cilia. To define "short cilia" we used a cutoff of two standard deviations from the wild-type average (7.48 µm, SD = 0.785). This gave a value of 5.91 µm. For convenience, this was rounded to the nearest whole number of 6 µm.

Statistical analysis for *C. elegans* data

Statistical analysis was performed using GraphPad Prism (version 10.1.2). A Shapiro–Wilk test was used to determine if the data were normally distributed. For parametric data, one-way ANOVA with a post hoc Tukey test was used to calculate *p*-values. Fischer's exact test was used to determine the statistical significance of categorical data. Graphs were made using Microsoft Excel or GraphPad Prism.

Reporting summary

Further information on research design is available in the Nature Portfolio Reporting Summary linked to this article.

Data availability

The source data for graphs and statistical quantifications used in this study are provided in the source data file. All other data that supports the findings of this study are available from the corresponding author upon reasonable request. Source data are provided with this paper.

REFEREnces

1. Goetz, S. C. & Anderson, K. V. The primary cilium: a signalling centre during vertebrate development. *Nat. Rev. Genet.* **11**, 331–344 (2010).
2. Ishikawa, H. & Marshall, W. F. Ciliogenesis: building the cell's antenna. *Nat. Rev. Mol. Cell Biol.* **12**, 222–234 (2011).
3. Anvarian, Z. et al. Cellular signalling by primary cilia in development, organ function and disease. *Nat. Rev. Nephrol.* **15**, 199–219 (2019).
4. Garcia, G. 3rd, Raleigh, D. R. & Reiter, J. F. How the ciliary membrane is organized inside-out to communicate outside-in. *Curr. Biol.* **28**, R421–R434 (2018).
5. Wheway, G., Nazlamova, L. & Hancock, J. T. Signaling through the primary cilium. *Front. Cell Dev. Biol.* **6**, 8 (2018).
6. Shinohara, K. & Hamada, H. Cilia in left-right symmetry breaking. *Cold Spring Harb. Perspect. Biol.* **9**, a028282 (2017).
7. Wallmeier, J. et al. Motile ciliopathies. *Nat. Rev. Dis. Prim.* **6**, 77 (2020).
8. Garcia-Gonzalo, F. R. & Reiter, J. F. Open sesame: how transition fibers and the transition zone control ciliary composition. *Cold Spring Harb. Perspect. Biol.* **9**, a028134 (2017).
9. Szymanska, K. & Johnson, C. A. The transition zone: an essential functional compartment of cilia. *Cilia* **1**, 10 (2012).
10. Chih, B. et al. A ciliopathy complex at the transition zone protects the cilia as a privileged membrane domain. *Nat. Cell Biol.* **14**, 61–72 (2011).
11. Garcia-Gonzalo, F. R. et al. A transition zone complex regulates mammalian ciliogenesis and ciliary membrane composition. *Nat. Genet.* **43**, 776–784 (2011).
12. Sang, L. et al. Mapping the NPHP-JBTS-MKS protein network reveals ciliopathy disease genes and pathways. *Cell* **145**, 513–528 (2011).
13. Hartill, V. et al. *Meckel-Gruber Syndrome*: an update on diagnosis, clinical management, and research advances. *Front. Pediatr.* **5**, 244 (2017).
14. Chen, C. P. Meckel syndrome: genetics, perinatal findings, and differential diagnosis. *Taiwan J. Obstet. Gynecol.* **46**, 9–14 (2007).
15. Parelkar, S. V. et al. Meckel-Gruber syndrome: a rare and lethal anomaly with review of literature. *J. Pediatr. Neurosci.* **8**, 154–157 (2013).
16. Baala, L. et al. The Meckel-Gruber syndrome gene, MKS3, is mutated in Joubert syndrome. *Am. J. Hum. Genet.* **80**, 186–194 (2007).
17. Iannicelli, M. et al. Novel TMEM67 mutations and genotype-phenotype correlates in meckelin-related ciliopathies. *Hum. Mutat.* **31**, E1319–E1331 (2010).
18. Khaddour, R. et al. Spectrum of MKS1 and MKS3 mutations in Meckel syndrome: a genotype-phenotype correlation. Mutation in brief #960. *Online Hum. Mutat.* **28**, 523–524 (2007).
19. Otto, E. A. et al. Mutation analysis of 18 nephronophthisis associated ciliopathy disease genes using a DNA pooling and next generation sequencing strategy. *J. Med. Genet.* **48**, 105–116 (2011).
20. Szymanska, K., Hartill, V. L. & Johnson, C. A. Unraveling the genetics of Joubert and Meckel-Gruber syndromes. *J. Pediatr. Genet.* **3**, 65–78 (2014).
21. Brancati, F. et al. Biallelic variants in the ciliary gene TMEM67 cause RHYNS syndrome. *Eur. J. Hum. Genet.* **26**, 1266–1271 (2018).
22. Brancati, F. et al. MKS3/TMEM67 mutations are a major cause of COACH Syndrome, a Joubert Syndrome related disorder with liver involvement. *Hum. Mutat.* **30**, E432–E442 (2009).
23. Huynh, J. M., Galindo, M. & Laukaitis, C. M. Missense variants in TMEM67 in a patient with Joubert syndrome. *Clin. Case Rep.* **6**, 2189–2192 (2018).
24. Lee, S. H. et al. Functional validation of novel MKS3/TMEM67 mutations in COACH syndrome. *Sci. Rep.* **7**, 10222 (2017).
25. Niehrs, C. The complex world of WNT receptor signalling. *Nat. Rev. Mol. Cell Biol.* **13**, 767–779 (2012).
26. Abdelhamed, Z. A. et al. The ciliary frizzled-like receptor Tmem67 regulates canonical Wnt/beta-catenin signalling in the developing cerebellum via Hoxb5. *Sci. Rep.* **9**, 5446 (2019).
27. Abdelhamed, Z. A. et al. The Meckel-Gruber syndrome protein TMEM67 controls basal body positioning and epithelial branching morphogenesis in mice via the non-canonical Wnt pathway. *Dis. Model Mech.* **8**, 527–541 (2015).
28. Lange, K. I. et al. Interpreting ciliopathy-associated missense variants of uncertain significance (VUS) in Caenorhabditis elegans. *Hum. Mol. Genet.* **31**, 1574–1587 (2022).
29. Leightner, A. C. et al. The Meckel syndrome protein meckelin (TMEM67) is a key regulator of cilia function but is not required for tissue planar polarity. *Hum. Mol. Genet.* **22**, 2024–2040 (2013).
30. Choi, Y. J. et al. Mutations of ADAMTS9 cause nephronophthisis-related ciliopathy. *Am. J. Hum. Genet.* **104**, 45–54 (2019).
31. Nandadasa, S. et al. Secreted metalloproteases ADAMTS9 and ADAMTS20 have a non-canonical role in ciliary vesicle growth during ciliogenesis. *Nat. Commun.* **10**, 953 (2019).
32. Kleifeld, O. et al. Identifying and quantifying proteolytic events and the natural N terminome by terminal amine isotopic labeling of substrates. *Nat. Protoc.* **6**, 1578–1611 (2011).
33. Nandadasa, S. et al. Degradomic identification of membrane type 1-matrix metalloproteinase as an ADAMTS9 and ADAMTS20 substrate. *Mol. Cell Proteom.* **22**, 100566 (2023).
34. Liu, D. et al. Structure of the human Meckel-Gruber protein Meckelin. *Sci. Adv.* **7**, eabj9748 (2021).
35. Rasmussen, M. et al. Targeted gene sequencing and whole-exome sequencing in autopsied fetuses with prenatally diagnosed kidney anomalies. *Clin. Genet.* **93**, 860–869 (2018).
36. Pir, M. S. et al. ConVarT: a search engine for matching human genetic variants with variants from non-human species. *Nucleic Acids Res.***50**, D1172–D1178 (2022).
37. Jumper, J. et al. Highly accurate protein structure prediction with AlphaFold. *Nature* **596**, 583–589 (2021).
38. Williams, C. L. et al. MKS and NPHP modules cooperate to establish basal body/transition zone membrane associations and ciliary gate function during ciliogenesis. *J. Cell Biol.* **192**, 1023–1041 (2011).
39. Williams, C. L., Masyukova, S. V. & Yoder, B. K. Normal ciliogenesis requires synergy between the cystic kidney disease genes MKS-3 and NPHP-4. *J. Am. Soc. Nephrol.* **21**, 782–793 (2010).

40. Somerville, R. P. et al. Characterization of ADAMTS-9 and ADAMTS-20 as a distinct ADAMTS subfamily related to Caenorhabditis elegans GON-1. *J. Biol. Chem.* **278**, 9503–9513 (2003).
41. Cook, S. A. et al. A mouse model for Meckel syndrome type 3. *J. Am. Soc. Nephrol.* **20**, 753–764 (2009).
42. Shim, J. W. et al. Hydrocephalus in a rat model of Meckel Gruber syndrome with a TMEM67 mutation. *Sci. Rep.* **9**, 1069 (2019).
43. Smith, U. M. et al. The transmembrane protein meckelin (MKS3) is mutated in Meckel-Gruber syndrome and the wpk rat. *Nat. Genet.* **38**, 191–196 (2006).
44. Abdelhamed, Z. A. et al. Variable expressivity of ciliopathy neurological phenotypes that encompass Meckel-Gruber syndrome and Joubert syndrome is caused by complex de-regulated ciliogenesis, Shh and Wnt signalling defects. *Hum. Mol. Genet.* **22**, 1358–1372 (2013).
45. Chapin, H. C., Rajendran, V. & Caplan, M. J. Polycystin-1 surface localization is stimulated by polycystin-2 and cleavage at the G protein-coupled receptor proteolytic site. *Mol. Biol. Cell* **21**, 4338–4348 (2010).
46. Qian, F. et al. Cleavage of polycystin-1 requires the receptor for egg jelly domain and is disrupted by human autosomal-dominant polycystic kidney disease 1-associated mutations. *Proc. Natl Acad. Sci. USA* **99**, 16981–16986 (2002).
47. Wei, W. et al. Characterization of cis-autoproteolysis of polycystin-1, the product of human polycystic kidney disease 1 gene. *J. Biol. Chem.* **282**, 21729–21737 (2007).
48. Woodward, O. M. et al. Identification of a polycystin-1 cleavage product, P100, that regulates store operated Ca entry through interactions with STIM1. *PLoS ONE***5**, e12305 (2010).
49. Yu, S. et al. Essential role of cleavage of Polycystin-1 at G protein-coupled receptor proteolytic site for kidney tubular structure. *Proc. Natl Acad. Sci. USA* **104**, 18688–18693 (2007).
50. Kim, H. et al. Ciliary membrane proteins traffic through the Golgi via a Rabep1/GGA1/Arl3-dependent mechanism. *Nat. Commun.* **5**, 5482 (2014).
51. Jungers, K. A. et al. Adamts9 is widely expressed during mouse embryo development. *Gene Expr. Patterns* **5**, 609–617 (2005).
52. Truong, H. M. et al. The tectonic complex regulates membrane protein composition in the photoreceptor cilium. *Nat. Commun.* **14**, 5671 (2023).
53. Shi, X. et al. Super-resolution microscopy reveals that disruption of ciliary transition-zone architecture causes Joubert syndrome. *Nat. Cell Biol.* **19**, 1178–1188 (2017).
54. Yang, T. T. et al. Superresolution pattern recognition reveals the architectural map of the ciliary transition zone. *Sci. Rep.* **5**, 14096 (2015).
55. Li, C. et al. MKS5 and CEP290 Dependent Assembly Pathway of the Ciliary Transition Zone. *PLoS Biol.* **14**, e1002416 (2016).
56. Wu, Z. et al. CEP290 is essential for the initiation of ciliary transition zone assembly. *PLoS Biol.* **18**, e3001034 (2020).
57. Kongkham, P. N. et al. The SFRP family of WNT inhibitors function as novel tumor suppressor genes epigenetically silenced in medulloblastoma. *Oncogene* **29**, 3017–3024 (2010).
58. Wuebken, A. & Schmidt-Ott, K. M. WNT/beta-catenin signaling in polycystic kidney disease. *Kidney Int.* **80**, 135–138 (2011).
59. Lancaster, M. A. & Gleeson, J. G. Cystic kidney disease: the role of Wnt signaling. *Trends Mol. Med.* **16**, 349–360 (2010).
60. Luo, J. et al. Wnt signaling and human diseases: what are the therapeutic implications?. *Lab Invest.* **87**, 97–103 (2007).
61. Lee, E. J. et al. TAZ/Wnt-beta-catenin/c-MYC axis regulates cystogenesis in polycystic kidney disease. *Proc. Natl Acad. Sci. USA* **117**, 29001–29012 (2020).
62. Li, A. et al. Canonical Wnt inhibitors ameliorate cystogenesis in a mouse ortholog of human ADPKD. *JCI Insight* **3**, e95874 (2018).
63. Lv, B. et al. E3 ubiquitin ligase Wwp1 regulates ciliary dynamics of the Hedgehog receptor Smoothened. *J. Cell Biol.* **220**, e202010177 (2021).
64. Brenner, S. The genetics of Caenorhabditis elegans. *Genetics* **77**, 71–94 (1974).
65. Paix, A. et al. High efficiency, homology-directed genome editing in caenorhabditis elegans using CRISPR-Cas9 ribonucleoprotein complexes. *Genetics* **201**, 47–54 (2015).
66. Arribere, J. A. et al. Efficient marker-free recovery of custom genetic modifications with CRISPR/Cas9 in Caenorhabditis elegans. *Genetics* **198**, 837–846 (2014).
67. Rawsthorne-Manning, H. et al. Confounds of using the unc-58 selection marker highlights the importance of genotyping co-CRISPR genes. *PLoS ONE***17**, e0253351 (2022).
68. Lange, K. I. et al. Interpreting the pathogenicity of Joubert syndrome missense variants in Caenorhabditis elegans. *Dis. Model Mech.* **14**, dmm046631 (2021).
69. Razzauti, A. & Laurent, P. Ectocytosis prevents accumulation of ciliary cargo in C. elegans sensory neurons. *eLife* **10**, e67670 (2021).

Acknowledgements

This work was funded by the National Institute of Health grant 5R01DK126804 and The Worcester Foundation grant awards to S.N. This work utilized SEM, TEM, and Ultramicrotomy equipment purchased from NIH awards S10RR021043, S10OD025113, and SI0OD021580. A TissueGnostics-SL slide scanner used in the study was funded by a Massachusetts Life Science Center, Bits to Bytes grant. S.B. was supported by a Wellcome Trust Clinical Training Fellowship (4Ward North Clinical PhD Academy, 203914/Z/16/Z). MRC project grants (MR/M000532/1 and MR/T017503/1) to C.A.J., and a bilateral BBSRC-SFI project grant (BB/P007791/1) to C.A.J. and O.B. supported this work. K.I.L. is supported by a Research Ireland grant (22/PATH-S/10738). We thank Patrick Laurent (Université libre de Bruxelles) for the TSP-6::mScarlet worms. We thank Professors George Witman and Piali Sengupta for their valuable input.

Author contributions

M.A., S.F., K.L., K.R., O.B., and S.N. conceived and designed the experiments. M.A., S.N., S.F., K.L., S.B., K.R., and M.S. performed the experiments. S.B., G.J.P., and C.A.J. provided reagents. M.A., K.L., and S.N. wrote the manuscript. All authors read, edited, and approved the manuscript.

Competing interests

The authors declare no competing interests

Additional information

Supplementary information The online version contains supplementary material available at https://doi.org/10.1038/s41467-025-60294-3.

Correspondence and requests for materials should be addressed to Sumeda Nandadasa.

Peer review information *Nature Communications* thanks Heon Yung Gee, Helen May-Simera, Bradley Yoder, and the other anonymous reviewer(s) for their contribution to the peer review of this work. A peer review file is available.